Chapter 1: Introduction

1.1: Background and Aim

The search for more useful ultra hard materials has led to another class of solid-state compounds, the oxynitrides. These compounds appear to be simple combinations of oxides and nitrides but exhibit new chemical and physical properties.[1-7] The first technological application of oxynitrides has been identified in the fields of ionic conductivity, as diffusion barriers, in integrated circuits, in bi-functional catalysis and recently as cutting tool materials.[1-7] At present transition oxynitrides are under production as novel inorganic pigments, replacing traditional toxic materials which typically contain Cd.[3] There has been increased interest in investigating the capability of these phases as structural ceramics owing to their good thermal, mechanical and chemical stability properties.[1] Although diamond is the hardest material known to mankind, its application as a ferrous alloy cutting tool is limited. This is due to its chemical interaction with iron. [8] Generally, the recent trend focuses on finding materials which are more useful than diamond rather than 'harder than diamond'. [9]

In view of this, the present work is aimed at investigating the potential of TaON and Zr_xTa_{1-x}-ON solid solutions as potentially hard materials. It is not only the hardness which is of importance here but also chemical resistance both oxidative and resistance to iron attack. This enables design of a material which can be useful in the machining of hard ferrous alloys. This expectation is reasonable in view of the hardness predicted for the cotunnite TaON and the chemical resistance that tantalum compounds possess in general.[1] Predictions made earlier suggest a phase transition from the ambient monoclinic phase which contains Ta seven coordinated by O and N to a higher symmetry cotunnite phase which contains nine coordinated Ta.[10] This transition is associated with an increase in the bulk modulus value from 280GPa to 369GPa for the respective TaON phases.[1] It is expected that there is an increase in hardness associated with this phase transition

following the hardness-bulk modulus relationship.[11] The bulk modulus value quoted for the high symmetry phase compares well with that of other ultra hard materials for example diamond (444GPa), c-BN (367GPa) and βC_3N_4 (427GPa).[11] However this transition occurs at a predicted pressure of 30GPa which is not accessible with commercially available equipment.[10] It has been suggested that TaON may undergo the same transitions as ZrO_2, i.e., monoclinic-tetragonal-cubic.[1] This is a temperature induced transition in the case of ZrO_2 with the tetragonal phase forming at 1440 K and the cubic phase at around 2640 K.[1] On the other hand it is not clear whether the TaON transformation is also temperature induced or not. TaON has been found to be prone to oxidation beyond 1000 ^{0}C through oxygen uptake to form Ta_2O_5 and N_2 gas thus making it difficult to observe the phase transitions for TaON above 1000 ^{0}C.[12] Thus this work is aimed at obtaining well sintered TaON and Ta-Zr(ON) materials and evaluating their mechanical properties. This will enable an assessment of the potential of these materials for wear part and cutting tool applications. In view of all the above an investigation was carried out to find out if the higher symmetry phases of the $Ta_{1-x}Zr_xO_{1+x}N_{1-x}$ system can be obtained at pressures of $\leq$5.5GPa (maximum attainable pressure for the commercially available apparatus used) starting with pure TaON and with subsequent Zr additions (x=0.2 and x=0.7) in the Ta-Zr system with a nominal composition of $Ta_{1-x}Zr_xO_{1+x}N_{1-x}$.

1.2: Project Overview

The present work was carried out with a view to investigate the possibility of obtaining hard materials for cutting tool applications based on the $Ta_{1-x}Zr_xO_{1+x}N_{1-x}$ system. This is described in five Chapters. In Chapter 1 a brief overview of the whole project is given. A compilation of the literature which enabled execution of the work is given in Chapter 2. This encompasses firstly a brief outline on Potentially Hard Materials, a very important section of the present work. A general discussion on transition metal-oxynitride compounds is given in section 2.1.1. This is followed by a concise discussion on the properties of TaON materials in section 2.1.2. The remaining sections of Chapter 2 focus mainly on the synthesis routes and general properties of hard materials such as hardness and fracture toughness. A contemporary and very important section on thermodynamic aspects of oxide powder reactions with ammonia is included. These considerations enabled the synthesis of the oxynitride materials. The experimental procedures used to accomplish this work are described in Chapter 3 i.e. equipment, chemicals and characterisation methods used. Chapter 4 gives a concise analysis of the results obtained at each stage of the synthesis route. A comparison was made with the results obtained from previous works. Lastly in Chapter 5 conclusions were drawn and an attempt was made to compare TaON materials with ZrO_2 ceramic materials.

Chapter 2: Literature review

2.1: Potentially Hard Materials

The quest for potentially hard materials has increased in the field of engineering materials over the past few years. At present there are several commercially available or potentially hard materials that possess quite attractive properties as summarised in Table 2.1.[11]

Material	Bulk modulus B_0 (GPa)	Knoop hardness (GPa)
$C_{diamond}$	442	75-100
cBN	367	45
Si_3N_4	220	17
SiC	211	33
B_4C	200	30

Table 2.1: Calculated bulk moduli B_0–Knoop hardness relationship of some existing and potential hard ceramic materials.

However hardness alone does not guarantee good wear resistance or tribological properties. A combination of high hardness, good fracture toughness, chemical stability and excellent high temperature mechanical properties confer good wear or tribological properties. For instance, although diamond has sufficed as the hardest known material, there is concern over its inability to resist iron attack at temperatures above 600^0C in machining applications.[13] Hence its use is mostly restricted to machining of non-ferrous materials. The discovery of cubic boron nitride in the 1960s helped address this problem but there still a large gap between these two materials.[13] This coupled with the expensive high pressure manufacturing routes used for both materials indicate that there is great need for cheaper and alternative hard materials. On the other hand attempts to improve the fracture toughness of existing ultra hard materials are not uncommon.

This has led to another hybrid of ceramic based materials, i.e., CMCs (Ceramic Matrix Composites), microstructure modified ceramics (ZTA-Zirconia Toughened Alumina) and nano-grained ceramics.[11]

A lot of research work has been done covering both the oxide and non-oxide based ceramics.[11] Recently there has been increased interest in transition metal oxynitrides. This has emanated from the possibility of attaining attractive properties such as high thermal, good electrical, mechanical and chemical stability properties.[11-16] On the other hand oxynitrides have been found to possess properties intermediate between oxides and nitrides which justify the increased interest in these compounds.[3] Tantalum oxynitride (TaON) is no exception in this regard. Since its discovery three decades ago there has been increased research dedicated to understanding this compound.[3,16]

Tantalum oxynitride is a potential candidate in many applications which include paint pigments for automotive hard coatings, high temperature applications and in the electronics industry(sensors, actuators).[2-3,14-18]Previous work by other researchers has shown relatively high calculated bulk moduli values, 278GPa for monoclinic TaON and 369GPa for the higher symmetry cotunnite phase.[1,4] These values are quite comparable with values obtained for other existing ultrahard materials.[11] However it is not known whether the higher symmetry phases can be obtained under practicable conditions owing to the pressure limitation of most high pressure apparatus. On the other hand TaON has been found to oxidise at temperatures $>1000^0$C. A pressure transition at 30GPa has been predicted in previous studies for pure TaON phase.[1,6] The $Ta_{1-x}Zr_xO_{1+x}N_{1-x}$ system has been predicted to undergo the same transitions as ZrO_2 with ZrO_2 transforming to the high pressure cotunitte phase at 15GPa.[1]

2.1.1: Transition metal-oxynitride compounds

The formation of oxynitride compounds has been found to occur by the partial substitution of oxygen anions in an oxide matrix with nitrogen anions. However, owing to the large triple bond in dinitrogen compared to double bonds in oxygen, nitrides and oxynitrides are less numerous than oxides.[19] Additionally the formation of nitrides and oxynitrides require elevated temperatures or high pressures, in order to surpass the high energy barrier for their formation.[20] Substitution of divalent oxygen anions by less electronegative trivalent nitrogen anions induces an increase in the degree of covalence in the compound.[19] The increase in charge can be compensated in two different ways. In the first case, a cross-substitution principle is applied which allows the same stoichiometry to be kept, and possibly the same structure, provided size conditions are obeyed.[19] In the second case, the anionic charge compensation is carried out according to two $2N^{3-}$ nitrogen anions replacing three $3O^{2-}$ oxygen anions.[19] This results in formation of an anionic vacancy for every two nitrogen atoms introduced as illustrated below.[19]

$$3O^{2-} = 2N^{3-} + 1V \qquad (2.1)$$

Since nitrogen is less electronegative than oxygen another consequence of the N/O substitution is an increase in the degree of covalence.[19] A characteristic feature is the strong colour change associated with the transition metal oxynitrides. In the ionic/covalent semiconducting compounds, the colour originates from the electronic interband transitions between the occupied valence band and the vacant conduction band.[19] An increased covalent character induces a decrease in the width of the optical band gap thus more covalent compounds tend to have lower band gap energies.[19]This increased covalence makes oxynitrides candidates as possible hard materials.

2.1.2: Crystal Structures and properties of TaON

The very first investigations of the ternary system Ta/O/N were performed by almost half a century ago.[21] Subsequent investigations by several other workers published a stoichiometrically precise TaON phase containing pentavalent Ta and an equal O: N ratio. Of interest is the ß-TaON phase, first reported by Brauer *et al.*[17] with a monoclinic (baddeleyite) crystal structure isostructural with baddeleyite ZrO_2.Work by other researchers however reported on non-stoichiometric TaON phases i.e. O: N ratio not equal to 1 and with O: N ratios that do not add up to unity as in the previous case but add up to two.[12] However in all cases there is a trend towards ordered crystallisation of monoclinic TaON. The structure shows complete ordering of the oxygen and nitrogen atoms in alternating layers perpendicular to the c-axis.[2] In this structure, Figure 2.1, every Ta atom is coordinated to four nitrogen atoms and three oxygen atoms with Ta-N (O) distances ranging from 1.99 to 2.15Å.[2,3] Thus every nitrogen atom is coordinated to four Ta atoms, while the oxygen atoms are coordinated to three Ta atoms. Neutron diffraction measurements by C.M. Fang *et al* [2] gave an equilibrium volume of 129.46$Å^3$ and a calculated bulk modulus of 278GPa.[2] A low temperature α-TaON modification with a complex hexagonal structure has been found to occur at temperatures lower than 800^0C.[2] The α to β transformation occurs at about 800^0C.[2]

	Lattice parameters					
	a/ Å	b/ Å	c/ Å	β/^{0}	Volume/$Å^3$	B*/GPa
Calculated	4.9878	5.0569	5.2063	99.50	129.46	278
Experimental	4.9581	5.0267	5.1752	99.64	127.16	

B*: calculated bulk modulus value.

Table 2.2: Neutron diffraction measurements showing calculated parameters and coordinates of atoms in β-TaON.[2]

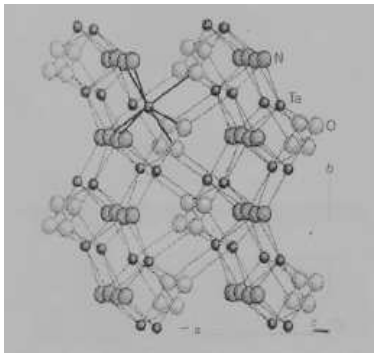

Figure 2.1: The crystal structure of β-TaON showing O/N ordering.[2]

A pressure induced phase transition was found to occur at about 30GPa to give a cotunnite crystal structure.[6] The cotunnite type is characterised by a ninefold coordination of the Ta atom.[6] The anions form trigonal prisms, capped on all rectangular faces around the central metal atom, Figure 2.2. There are four oxygen atoms and five nitrogen atoms bonded to the tantalum with Ta-N(O) distances of approximately 2.04 to 2.33Å where the latter is the average Ta-Ta bond length.[6]The pressure induced transition is associated with disordering of the O/N anions to a nine coordinated structure.

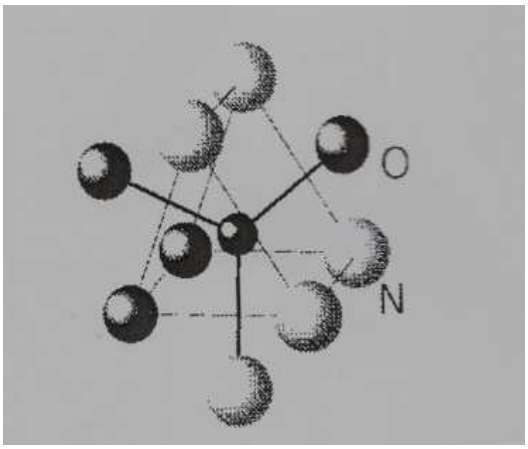

Figure 2.2: High pressure cotunnite structure of TaON. [6]

2.1.3: Ta_2O_5-ZrO_2 system

The present work involves the synthesis of new transition-metal oxynitrides containing both zirconium and tantalum. This calls for an in-depth understanding of the Ta_2O_5-ZrO_2 system. The solid solubility of Ta_2O_5 in ZrO_2 has been studied at temperatures of up to 1700^0C.[22] At ambient temperature, a mixture of monoclinic ZrO_2 and $Ta_2Zr_8O_{21}$ was found in the ZrO_2 rich part of the Ta_2O_5-ZrO_2 system.[23] In general defect chemistry predicts the formation of excess anions by alloying ZrO_2 with a small amount of metal oxide with a valence higher than four.[23] This is clearly outlined by the equation below;

$$Ta_2O_5 = 2Ta_{Zr} + 4O_O^x + O_i \qquad (2.2)$$

In equation 2.2 Ta_{Zr}, O_O^x and O_i denote tantalum cation replacing zirconium cation, oxygen anion at a regular oxygen site and the excess oxygen anions respectively.

From defect chemistry the incorporation of nitrogen into an oxygen excess ZrO_2 material results in an annihilation of the excess ions through equation (2.3) below;[23]

$$O_i + V_O^{\cdot\cdot} = O_O^x \qquad (2.3)$$

$V_O^{\cdot\cdot}$ denote the oxygen vacancy in the anionic sub lattice.
Thus depending on the relative amounts of Ta_2O_5, it should be possible to control the defect chemistry of such materials.[23]

Figure 2.3. reveals that solid solutions of the two oxides occur in two regions, i.e., phase V constituting ~14.3%-33.0 mol% Ta_2O_5 and Ta_2O_5ss constituting ~80-100 mol% Ta_2O_5 respectively.[22] Thus outside these two regions there is no complete solid solubility. Either excess ZrO_2 or Ta_2O_5 forms in the mixture.

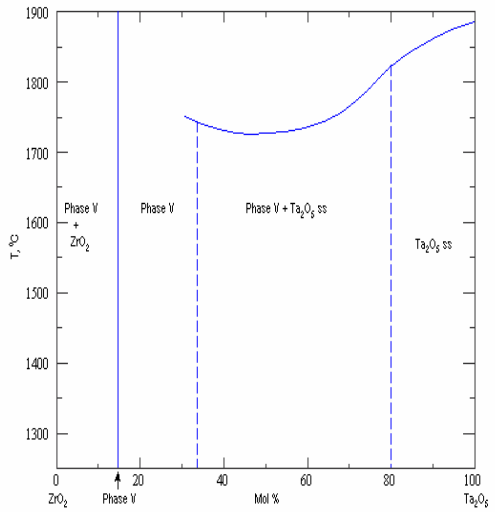

Figure 2.3: The ZrO_2-Ta_2O_5 phase diagram showing miscibility limits of ZrO_2 in Ta_2O_5.[22]

2.1.4: Tantalum-Zirconium Oxynitrides

These compounds are obtained by cationic substitutions in the TaON matrix to form a range of compounds with the general formula $Zr_xTa_{1-x}O_{1+x}N_{1-x}$. This is a consequence of the replacement of tantalum ions by the larger zirconium ions (Shannon-Prewitt ionic radii for Ta^{5+} =0.69 Å and Zr^{4+}=0.78 Å) (as cited in [3]). Rietveld refinement of $Zr_{0.4}Ta_{0.6}O_{1.4}N_{0.6}$ has shown a baddeleyite (monoclinic) type structure with Ta-N(O) distances of approximately 2.12 -2.15 Å showing a decrease in the degree of covalence with the incorporation of zirconium.[3] A comparison with the Ta-N(O) cotunnite bond distances shows that incorporation of zirconium is effective in increasing the Ta-N(O) bond length.

2.2: Chemical Synthesis of ceramic materials

Recent years have seen the emergence of newer and more versatile chemical processing techniques. These are aimed at addressing limitations associated with conventional mechanical processing techniques. One such method is the sol-gel process. The technique can be applied to obtain a wide range of multi-component

compounds including oxides, nitrides and carbides. Despite being costly it has brought with it improvements in chemical homogeneity, lower impurity levels and lower calcination temperatures owing to reduced diffusion distances which are rarely achievable with conventional mechanical and mixing methods.[3,14-17] A common example of the sol gel process is the method used in synthesis of silicates (TEOS-tetraethoxysilane and TMOS-tetramethoxysilane) based materials.[27]

2.2.1: Sol-gel processing

The basic principle of sol-gel synthesis is the controlled hydrolysis of a metal-organic compound (alkoxide) in an organic solvent. [7]Preparation of multicomponent oxides involves mixing of alkoxides in an alcohol and a component unavailable as an alkoxide can be introduced as a salt so that the resulting solution has the required composition. [24-25] It is preferable to use lower straight chain alcohols as straight forward and faster reactions will occur. Long chain alcohols are associated with side reactions which can lead to lower alkoxide yield.[24-26] The process proceeds via a complex interaction of hydrolysis and condensation reactions forming initially colloidal agglomerates which develop to a polymeric state called a gel during a gelation process.[25,27] The characteristics and properties of a particular sol-gel inorganic network are related to a number of factors that affect the rate of hydrolysis and condensation reactions such as pH, temperature, reagent concentrations, catalyst nature, water/alkoxide ratio (R), aging temperature and time. Of all the factors pH, nature and concentration of catalyst, water/alkoxide ratio(R) and the temperature have been found to be the most vital.[27] Control of these factors makes it possible to vary the structure and properties of the sol-gel derived inorganic network over wide ranges. There are two main steps in sol-gel which are described below. A successful sol-gel is governed by overcoming constraints within these two steps.

2.2.1.1: Hydrolysis

Hydrolysis is carried out under controlled conditions of pH, water added, alkoxide and alcohol concentration. Generally there is replacement of the alkyl group (R) with the hydroxyl group (OH). This occurs by the nucleophilic attack of the oxygen contained in water on the metal atom via the reaction; [27]

$$M(OR)_Z + H_2O = M(OH)(OR)_{Z-1} + ROH \qquad (2.4)$$

This is a stepwise reaction where M $(OR)_z$ is the metal alkoxide with metal M of valence z and R is an alkyl group.

2.2.1.2 Factors affecting hydrolysis

- ***Nature and concentration of catalyst***

Hydrolysis can occur without addition of external catalysts, it is however most rapid and complete when they are used.[27] Mineral acids (HCl) and ammonia are most commonly used, other catalysts utilized are acetic acid, KOH, amines, KF and HF.[2, 27] It has been observed that the rate and extent of the hydrolysis reaction is most influenced by the strength and concentration of the catalyst.[27]

- ***Acid catalysed mechanism***

In acid catalysed reactions the likely mechanism is the protonation of the alkoxide group in a first rapid step as suggested by *Mauritz et al* [27] and co-workers. Electron density is withdrawn from the metal atom making it more electrophilic and thus more susceptible to attack from water.

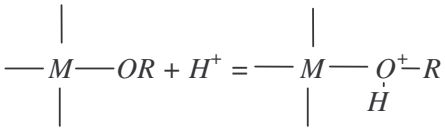

(2.5)

This results in the formation of a penta-coordinate transition state which decays by displacement of an alcohol and inversion of the metal tetrahedron.

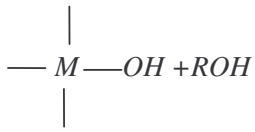

$$\text{—}M\text{—}OH + ROH \qquad (2.6)$$

- ***Base-catalysed mechanism***

Under basic conditions it is likely that water dissociates to produce hydroxyl anions in a rapid first step. The hydroxyl anion then attacks the metal atom. The same mechanism has been proposed in which the –OH displaces –OR with inversion of the metal tetrahedron.[27]

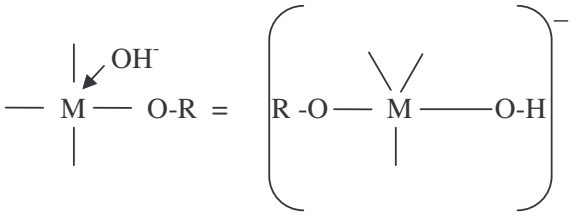

$$\text{—}M\text{—}O\text{-}R + OH^- = \left[R\text{-}O\text{—}M\text{—}O\text{-}H\right]^- \qquad (2.7)$$

In this case the active OH^- displaces the –OR group to form the metastable tetrahedron which again decomposes to form products as in equation 2.6. Clearly in both cases it is the active H^+ and OH^- which initiate the reactions.

- ***Water/alkoxide ratio (R)***

The obvious effect of the increasing the magnitude of R is the acceleration of the hydrolysis reaction. Higher values of water/alkoxide ratios cause more complete hydrolysis before significant condensation occurs.[27] Generally, with understoichiometric additions of water (R«2) the alcohol producing condensation reaction is favoured, whereas the water forming condensation reaction is favoured when (R≥2.28).

2.2.2: Condensation

Generally involves the polymerisation processes described by three stages namely:

i.) Polymerisation to form particles

ii.) Growth of particles.

iii.) Linking of particles into chains, then networks that extend throughout the liquid medium thickening into a gel.

A number of factors affect the rate of condensation such as temperature, time of reaction, properties of starting materials (e.g. diffusivities, reactivities) and catalyst nature and concentration. Particle growth however has been observed to be mainly depended on the temperature, nature and concentration of the catalyst.[24, 27] Growth occurs until the difference in solubility between the smallest and the largest particles becomes indistinguishable.[24, 27] Condensation results in the formation of (-M-O-M-) metal -oxygen-metal bonds by self condensation or cross condensation for two/more metal systems via the water/alcohol condensation reactions:

Alcohol condensation reaction

$$M(OR)_z + M(OR)_{z-1}(OH) = (RO)_{z-1}\text{-}M\text{-}O\text{-}M\text{-}(OR)_{z-1} + ROH \quad (2.8)$$

Water condensation reaction

$$2M(OH)(OR)_{z-1} = 2(RO)_{z-1}\text{-}M\text{-}O\text{-}M\text{-}(OR)_{z-1} + H_2O \quad (2.9)$$

2.2.3: Drying

This is aimed at driving off trapped water, alcohols and chemically adsorbed hydroxyl functional groups from the network. Several methods have been used in previous research works of a similar nature. One route involves heating in vacuum at ~100^0C for 48hrs to drive off first the water trapped followed by heating at higher temperatures typically 600^0C to drive off alcohols and other

remaining volatiles to produce a dried gel referred to as xerogel.[5] Another route is to calcine the gel at about 800^0C in oxygen to form a semi-dense oxide.[25]In practice the calcination temperature can be obtained from thermogravimetry.

2.3: Synthesis of oxynitride compounds

The synthesis of oxynitrides do not follow well established rules.[19] Thus each system is likely to react differently as a function of several parameters, that is, intrinsic (properties of reacting components) or extrinsic (operating parameters).[19]Solid/gas reactions are the most usual routes to oxynitrides, thermal nitridation is generally carried out.[19]

2.3.1: Reaction of oxides with flowing ammonia

Ammonia is often used as a nitriding agent instead of nitrogen gas.[28] Previous studies have shown that the use of nitrogen as a nitriding agent requires comparatively higher operating temperatures and pressures whereas with the use of ammonia nitridation can be achieved under atmospheric pressure at temperatures of 700-1000^0C for Ta_2O_5.[5,28] There is lower reactivity of N_2 in metals at 1atm.[28] Attempts to produce iron nitrides by other researchers at temperatures above 1000^0C and pressures of up to 10^9Pa (10^4atm) in nitrogen were not successful but was successfully done at 500^0C using ammonia flow at 1atm pressure.[28] This clearly indicates that the nitrogen reactivity in ammonia must be enormously high. Two important trends have been observed in previous studies;

i. The use of ammonia makes the reaction period shorter.
ii. The nitride is formed at considerably lower temperatures.[28]

The nitrogen partial pressure given by equation (2.10) below and is more properly termed nitrogen fugacity, with a numerical value in the hundreds or

thousands of atmospheres.[12,28] This can be explained with the aid of the equations below;

$$NH_3 = \frac{3}{2}H_2 + \frac{1}{2}N_2 \qquad (2.10)$$

$$K_P = \frac{(P_{NH3})}{(P_{N2})^{\frac{1}{2}}(P_{H2})^{\frac{3}{2}}} \qquad (2.11)$$

In equation (2.11) the terms K_P, P_{NH3} P_{N2} and P_{H2} denote the equilibrium constant, partial pressures of, ammonia, nitrogen and hydrogen respectively.

However the decomposition or 'cracking' reaction does not occur to a noticeable extent as long as ammonia does not come in contact with a metal catalyst.[12, 28] This explains the importance of using high surface area starting powders in nitridation reactions which are more effective in catalysing the reaction. The equation (2.11) above which relates the equilibrium partial pressures of the gases to the equilibrium constant which has often been used to predict the nitrogen activity of unstable ammonia.[28] The extremely high nitrogen activity can only be explained from the equilibrium viewpoint rather than from a kinetic viewpoint.[28] However no exact thermodynamic treatment of why unstable flowing ammonia exhibits an extremely high nitrogen activity has been reported thus the use of the equilibrium constant Kp can work as a good approximation of the nitrogen activity in the system.[28]

Ammonia acts as both a reducing and nitriding agent.[28] The ammonia flow rate depends on the reaction temperature, that is, there is a tendency for increased flow rates at higher temperatures.[28] A reducing character may predominate or not, depending on the reaction temperature and nature of the precursor oxide powder.[12] This dual behaviour of nitriding and reducing is very important for the ammonolysis reaction.[12] The success of the solid/gas ammonolysis depends

highly on the nature of the precursors, that is, intrinsic properties. The preparation of ammonolysis precursors by solid state methods has shown limits regarding their homogeneity and reactivity.[12] This is because the specific surface areas of such precursors are generally low inducing low reactivity.

2.3.2: Thermodynamic aspects of oxide powder/ammonia reactions

When a porous solid material is brought into contact with ammonia, the following reactions are possible;

$$NH_3 = \frac{1}{2}N_2 + \frac{3}{2}H_2 \qquad (2.12)$$

$$NH_3 + \frac{3}{2}O(in\_oxide) = N(in\_oxynitride) + \frac{3}{2}H_2O \qquad (2.13)$$

$$NH_3 = 3H(in\_hydride) + \frac{1}{2}N_2 \qquad (2.14)$$

Reaction (2.12) is the dissociation of ammonia into H_2 and N_2 usually catalysed by the solid. Reactions (2.13) and (2.14) represent nitride and hydride formation by action of ammonia respectively. At equilibrium ammonia always co-exist with N_2 and H_2 and the partial pressures of the three gases may be determined by the equilibrium constant of reaction (2.12) at a given temperature.[28] If the total pressure is given, reaction (2.13) or (2.14) occur in parallel with reaction (2.12) and under these conditions ammonia may act as a nitriding or hydriding agent depending on the reaction prevailing.[28] However the dissociation of ammonia can be suppressed to a great extent by using a flow method.[28] By flowing ammonia gas its extent of dissociation may be kept below the equilibrium dissociation and complete suppression of ammonia dissociation is impossible.[28] The extent of dissociation depends upon several experimental conditions such as the temperature of the hottest zone, temperature distribution, flow rate of ammonia, surface properties of the walls of the reaction tube and specimen and the geometric construction of the whole system.[28] In general as the flow rate is

reduced, the extent of dissociation approaches its equilibrium value. Reaction 2.13 represents a partial equilibrium between flowing ammonia and metal nitride. At partial equilibrium the following relation must hold;

$$\mu_{NH_3} = \mu(N\_in\_oxynitride) + \frac{3}{2}\mu_{H_2} \tag{2.15}$$

and

$$\mu_{NH_3} = \Delta G^0_{NH_3} + RT \ln P_{NH_3} \tag{2.16}$$

$$\mu_{H_2} = RT \ln P_{H_2} \tag{2.17}$$

P_{NH_3} and P_{H_2} are the partial pressures of NH_3 and hydrogen respectively in atmospheres and $\Delta G^0_{NH_3}$ is the standard free energy of formation of NH_3 at 1atm pressure and μ represents the chemical potentials of the specified reagents. Substituting (2.16) and (2.17) into (2.15) will result in the equation below;

$$\mu(N\_in\_oxynitride) = \Delta G^o_{NH_3} + RT \ln\left(\frac{P_{NH_3}}{P_{H_2}^{\frac{3}{2}}}\right) \tag{2.18}$$

the chemical potential μ *(N in nitride)* is related to the nitrogen activity a_N by the relation;

$$\mu \text{ (N in oxy nitride)} = RT \ln (a_N) \tag{2.19}$$

thus from [2.2.9] and [2.2.10] the nitrogen activity can be equilibrated with;

$$a_N = \left(\frac{P_{NH_3}}{P_{H_2}^{\frac{3}{2}}}\right) \exp\left(\frac{\Delta G^o_{NH_3}}{RT}\right) \tag{2.20}$$

the free energy of formation is related to the equilibrium constant K_p by equation (2.21) below;

$$\Delta G^{o}_{NH_3} = -RT \ln K_p \tag{2.21}$$

Thus the nitrogen activity a_N is given by;

$$a_N = \frac{1}{K_p}\left(\frac{P_{NH_3}}{P^{\frac{3}{2}}_{H_2}}\right) \tag{2.22}$$

The rate of dissociation α is a function of the speed v of flowing ammonia and related through the equation below;

$$\alpha = F(v)\ (\leq \alpha_{max}) \tag{2.23}$$

and at equilibrium;

$$(1-\alpha)NH_3 = \frac{3}{2}\alpha H_2 + \frac{\alpha}{2}N_2 \tag{2.24}$$

If p is the total pressure of the system then the total pressure as a function of the rate of dissociation is given by;

$$p = \left\{(1-\alpha) + \frac{3}{2}\alpha + \frac{\alpha}{2}\right\} = (1+\alpha) \tag{2.25}$$

thus the partial pressures of NH_3, H_2, *and* $N2$ are related to the dissociation rate by;

$$P_{NH_3} = \frac{(1-\alpha)}{(1+\alpha)} \tag{2.26}$$

$$P_{H_2} = \frac{3\alpha}{2(1+\alpha)} \tag{2.27}$$

$$P_{N_2} = \frac{\alpha}{2(1+\alpha)} \qquad (2.28)$$

The activity of nitrogen a_N is correlated with the rate of dissociation α, which depends on the speed of flowing ammonia through the hot reaction zone can be expressed by the equation;

$$a_N = \frac{1}{K_p} \frac{(1-\alpha)\left[2(1+\alpha)\right]^{\frac{3}{2}}}{(3\alpha)^{\frac{3}{2}}(1+\alpha)} \qquad (2.29)$$

simplifying gives;

$$a_N = 0.544 K_P^{-1} \frac{(1-\alpha)(1+\alpha)^{\frac{1}{2}}}{\alpha^{\frac{3}{2}}} \qquad (2.30)$$

Clearly from (2.21) the activity a_N approximates a lower value as the rate of dissociation α increases and conversely it approximates a higher value as α decreases. It can be concluded that at higher flow rates the activity of nitrogen is higher and it is highly likely to obtain the fully nitrided phases such as Ta_3N_5 and at lower flow rates TaON formation is more favourable. It can be seen that the resultant product is determined by manipulating the value of the nitrogen activity through the control of the flow rate. There is also a great dependence of the activity on the temperature. As previously discussed the temperature determines the speed of the ammonia in the hot zone thus there is a gradual increase in the activity with increasing temperature.[28] In general the activity of the nitrogen is higher at higher temperatures. The relationship between the nitrogen activity and the extent of dissociation at several temperatures is summarised in the graph below. Clearly there is a decrease in the nitrogen activity a_N with increase in the degree of dissociation of the ammonia decomposition reaction, equation 2.13. In other words, higher nitrogen activities are obtainable at lower dissociation values, α. In this case a state of instability is created where the dissociation

equilibrium $NH_3 = \frac{1}{2}N_2 + \frac{3}{2}H_2$ is not reached. The high nitrogen activity exhibited by flowing ammonia may arise due to this instability.[28]

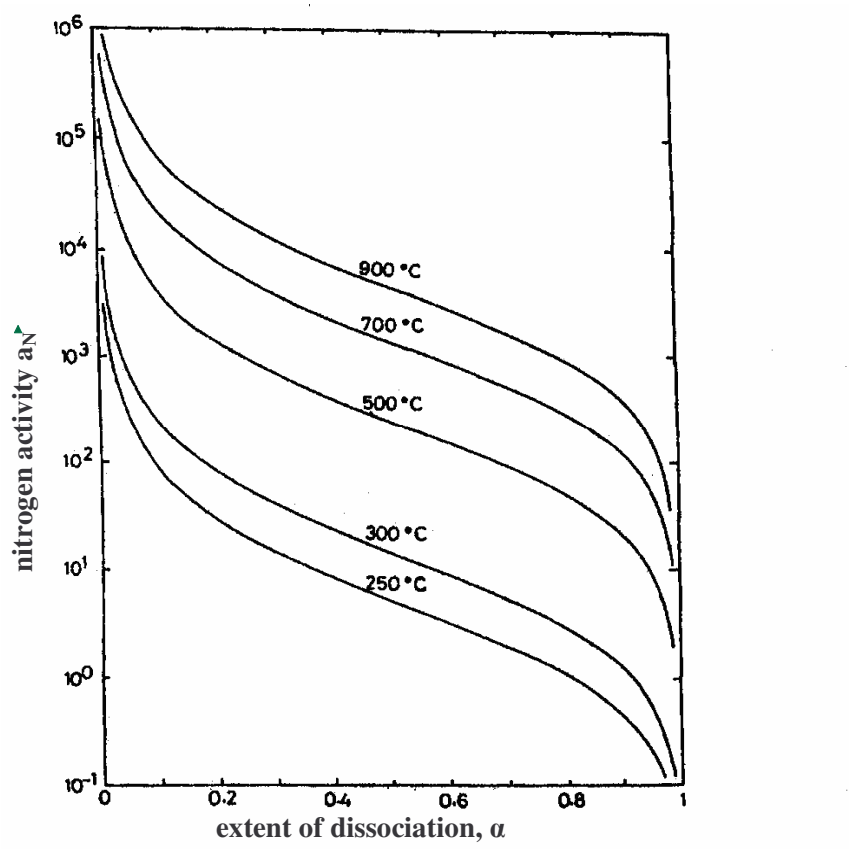

Formatted: Font: Bold, Complex Script Font: Bold

Figure 2.4: The relative nitrogen activity (a_N) exhibited by flowing ammonia as a function of dissociation (α) at various temperatures.[28]

There has been a trend towards the use of wet ammonia to obtain the TaON phase by many researchers.[12, 17, 20, 29] A thermodynamic consideration may be used to explain the instability of the TaON. Orhan *et al* [20] used oxidative drop solution calorimetric method to determine the heat of formation of nitride and oxynitrides

of tantalum. The standard enthalpies of reaction were determined for Ta_2O_5, TaON, and Ta_3N_5;

$$Ta_2O_5 + 2NH_3 = 2TaON + 3H_2O \qquad \Delta H_r = +9.25kJ/mol\ at\ 298K \quad (2.31)$$

$$3Ta_2O_5 + 10NH_3 = 2Ta_3N_5 + 15H_2O \quad \Delta H_r = +610.0kJ/mol\ at\ 298K \quad (2.32)$$

$$3TaON + 2NH_3 = Ta_3N_5 + 3H_2O \quad \Delta H_r = +291.12kJ/mol\ at\ 298K \quad (2.33)$$

The energy involved at the onset of nitridation at ~1173K(900^0C) is more than enough to pass the TaON formation stage.[20] Thus the use of wet ammonia has been used to set up an equilibrium between the forward nitridation reaction and the reverse hydrolysis reaction.[20]

2.4: Sintering of ceramic materials

The bulk sintering of most nitride based compounds is quite difficult owing to oxidation occurring at temperatures too low to obtain well sintered bodies. TaON is one such material. This has a negative impact on the sinterability of TaON since the driving force of sintering is a function of surface free energy, temperature and pressure of the system. At low temperatures and low pressures there is not enough energy available to allow for diffusional mass transport in solid state sintering of most materials.[30] This is in accordance with the temperature dependence of the diffusion coefficient D on temperature which has the following Arhenius relationship.[19]

$$D = D_0 \exp\left(-\frac{\Delta H}{RT}\right) \qquad (2.34)$$

where D_0 is a constant dependent on the atomic planar distance λ and the mean frequency of vibration v and is equivalent to v $\lambda^2/6$ exp $\{\Delta S/K\}$.ΔH is the enthalpy change associated with overcoming the diffusion energy barrier and T the absolute temperature. Clearly the driving force for densification is temperature

dependent. A conventional remedy which has been utilized to aid in the sintering of nitride based compounds over the years is the use of sintering additives.[30] These form a liquid phase slightly below the sintering temperature thus providing a high diffusivity pathway for the subsequent solution-diffusion-precipitation processes.[30] This forms the basis of liquid phase sintering conventionally used for Si_3N_4 and SiC materials. However owing to the lack of literature on the sintering of TaON it would be more beneficial to investigate and understand the solid state sintering behaviour of this phase prior to the addition of such aids which could introduce secondary phases in the system.

One other method of interest is gas pressure sintering (GPS). This is based on the use of nitrogen gas to suppress the decomposition of nitride based compounds at high temperatures. This has been carried out successfully on Si_3N_4 compounds which have been sintered at temperatures well above the decomposition temperature of ~1800^0C.[31] This approach could possibly be applied to the TaON phase since an equilibrium state can be set up to suppress the oxidation of TaON at temperatures above 1000^0C.[12] The application of mechanical hot pressing(HP) and a subsequent gas pressure hot isostatic pressing (HIP) is also an effective way of improving the rate of densification provided only closed porosity at low levels (approximately <2%) is obtained after hot pressing (HP).[7,31] This is well articulated by the various creep equations which relate the creep rate (linear strain rate) to the densification rate (volumetric strain rate). Generally during hot pressing (HP) the density D of the sample increases with a decrease in thickness, L. The variables D and L are related by;

$$\frac{M}{A} = LD = L_0 D_0 = L_f D_f \qquad (2.35)$$

where M is the sample mass, A the cross sectional area of the die and the subscripts $_0$ and f refer to initial and final values. Differentiating equation (2.35) yields;

$$L\frac{dD}{dt} + D\frac{dL}{dt} = 0 \qquad (2.36)$$

and

$$-\frac{1}{L}\frac{dL}{dt} = \frac{1}{D}\frac{dD}{dt} \qquad (2.37)$$

This equation relates the linear strain rate of the body during hot pressing (HP) to its densification rate. This is in accordance with the Nabaro-Herring creep equation which in essence argues that self diffusion within the crystal will cause the solid to deform in an attempt to relieve stress.[25] The creep being a result of atoms diffusing from interfaces subjected to a compressive stress (where they have a higher chemical potential) towards those subjected to a tensile stress (lower chemical potential). The atomic flux, $\acute{\varepsilon}_c$ by Herring gave the relationship:

$$\varepsilon_c' = \frac{40}{3}\left(\frac{D_e \Omega P_a}{G^2 kT}\right) \qquad (2.38)$$

where D_e is the lattice diffusion coefficient, Ω is the atomic volume, P_a is the applied stress, G is the grain size, k is the Boltzmann constant and T is the absolute temperature. The value $\acute{\varepsilon}_c$ is the creep rate equivalent to the linear strain rate (1/L) dL/dt in (2.28) above. Clearly there is a high dependency of densification rate on the grain size G and the applied pressure Pa. This has been used with success in ultra high pressure sintering especially for materials which are difficult to compress (materials with high bulk moduli values) typically diamond and cubic boron nitride.[13] This is an expensive process for obtaining sintered bodies owing to the expensive equipment required to achieve sintering.

2.4.1: High pressure sintering

In most systems there is limited amount of control over material parameters such as diffusion and vapour transport rates, interfacial energies and phase

compositions, which may or may not be compatible with densification by solid state.[26] High pressure sintering is an effective approach to densification which supplements the capillary driving force with an externally applied pressure, Figure 2.3.1. [26] In principle the applied pressure, P_a is magnified at the contact area between particles, this pressure is added to the capillary pressure to give a higher densification pressure.[26] The applied pressure increases the driving force for densification but not for coarsening, because the pressure is applied to the grain boundaries and does not directly affect the neck curvature which drives coarsening properties.[26] Thus an external pressure promotes densification over coarsening processes. This is illustrated in the diagram below where the total pressure, P_T is given by;

$$P_T = \frac{total \quad force}{\pi x^2} \approx \frac{P_a (2r)^2}{\pi N x^2} \tag{2.39}$$

P_a is the applied pressure, x is the grain boundary radius, N is the total number of grains and r is the particle radius.

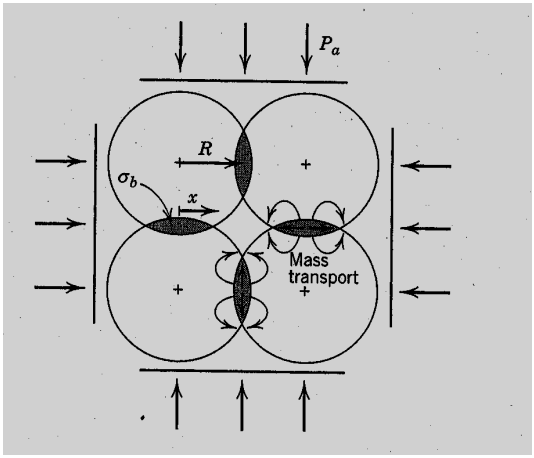

Figure 2.5: Microscopic illustration of high pressure sintering.[26]

2.4.1.1: High pressure sintering apparatus

Since the discovery of high pressure apparatus in the early 1950s there has been progressive developments over the years.[32] In March 1952,P.W Bridgman described an ingenious single stage apparatus for producing pressures of up to 100 000kg/cm^2 (9.68*10^4 atm) using carboloy anvils.[32] Recent developments have seen the emergence of higher volume apparatus, 'the belt' which can maintain pressures of up to ~6GPa at temperatures in excess of 2000^{0}C for several hours.[32] The equipment makes use of tungsten carbide pistons that push into opposite ends of a specially shaped tungsten carbide chamber.[32-33] Axial motion of the conical pistons in and out of the chamber is accomplished while still maintaining a pressure seal by use of a 30degree conically shaped sandwich pyrophyllite gasket.[32] The pyrophyllite gasket is also used as a pressure transmitting medium, thermal insulator and electrical insulator.[32] The centre of the assembly ,where the sample is located ,sustains more load than the outer regions.[32-33] There is a gradual drop of pressure along the gasket giving a multi-staging effect that is likened to building one piece of pressure apparatus inside another.[32] The gasket can be taken as a 'big shell' built from several other subshells at different pressures. The outermost shell has the least pressure with support coming from above and below due to friction and atmospheric pressure from outside support.[32] The outermost shell gives support at the back of the next inner shell. This coupled with the upper and lower frictional support gives even greater pressure.[32] This results in a successive increase in the pressure towards the centre of the gasket.

The thrust of the conical pistons develops compression in the chamber also obtaining a multistaging effect.[32] In most cases the pressure application is done simultaneously with the heating process which is achieved by passage of an electric current through the heating spool.

2.5: Definition and properties of hard and ultra hard ceramic materials

2.5.1: Ultrahard Materials

Generally the definition of ultrahard materials is that their hardness values are comparable to that of diamond.[11] Often the hardness of such materials exceeds 40GPa.[11] Among all known single phase compounds only diamond and cBN exceed this value. Hardness can be defined as the resistance of a material to elastic and plastic deformation.[34] This deformation begins when the shear component of the applied stress exceeds the yield stress.[11] Hardness is strongly influenced by residual stresses, toughening phases, microstructural textures, grain size, applied load, porosity and structure and composition of grain boundaries. [11] The hardness value is given by a ratio of the applied load to the area of surface contact of a hard indenter, usually diamond, loaded perpendicular to a planar surface of material under test. The measured hardness value of any material depends on parameters associated with the test method and indenter geometry.[34] It varies with the applied load, indenter shape and dimensions, microstructure and prior history of the material, loading rate, the environment and the test temperature.[34-35] Thus in order to compare hardness values of different materials, the specific test method and test conditions have to be described carefully.[11]

Theoretical attempts to describe hardness in terms of the elastic bulk or shear moduli of an ideal solid are not uncommon. The elastic moduli are an intrinsic mechanical property of a material dominated by the strength of the chemical bond between the atoms.[11] The high elastic moduli of ultra hard materials reflect the strong chemical bonds between the atoms. These bonds are predominately covalent in nature. In general, ionic/covalent bonds deform less than metallic bonds under a given external force.[11] Thus the theoretical hardness assumes

higher values at greater elastic moduli values. This 'theoretical' hardness is proportional to the reciprocal value of the bulk modulus, B.[11]

There is a relationship between the bulk modulus B, the applied stress ψ and ε the elastic strain , from Hooke's law;

$B = d\psi/d\varepsilon$ (2.40)

and from the binding energy E_b, bond length and stress relation

$\psi = (dE_b/da)$ (2.41)

Clearly there is a direct relationship between the bulk modulus B and the binding energy E_b and the interatomic bond distance a is described by the equation;

$B = (d^2E_b/da^2)$ (2.42)

Thus high bond energy means high electron density between the atoms as in non-polar covalent bonds between atoms of small radii of the first period hence the high hardness values attained by compounds of these elements.[11] A more common bulk modulus-bond length relationship which has been used to predict the theoretical hardness values of most existing and potential ultra hard materials is given by the equation below.[11]

$$B(GPa) = \left(\frac{N_c}{4}\right)\left(\frac{1971 - 220\lambda}{d^{3.5}}\right) \quad (2.43)$$

where N_c is the coordination number, d is the bond length (Å) and λ is an empirical parameter measuring the polarity of the bond. For non-polar covalent bonds such as in diamond λ =0, whereas in other compounds such as cBN, Si_3N_4 and SiC, λ >0 hence the lower bulk moduli and hardness values for these compounds compared to diamond. Figure 2.6 below show Knoop hardness and bulk moduli relationships for some potential and existing ultra hard materials obtained for single crystals using the relation (2.43).

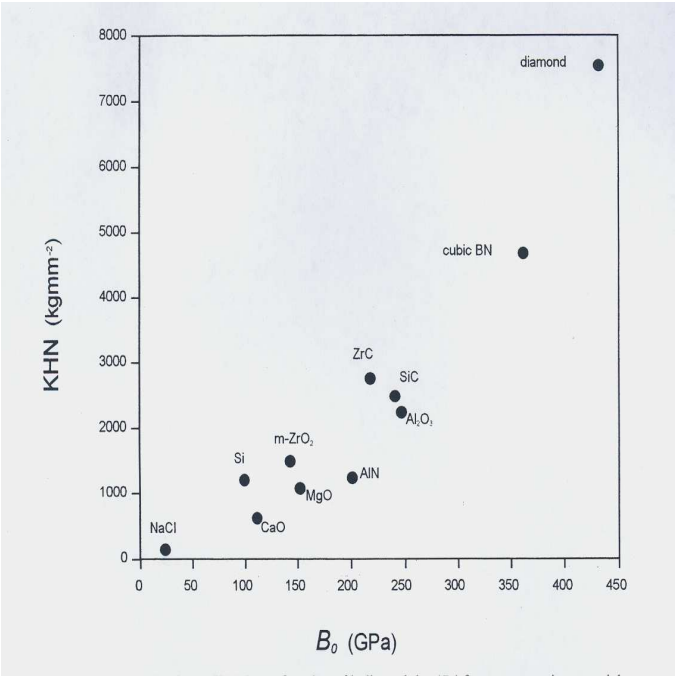

Figure 2.6: Knoop hardness KHN ($kgmm^{-2}$) plotted against calculated bulk moduli B_0 (GPa) of some common materials.[11]

However it has been argued that materials deform plastically only when subjected to a shear stress.[11] Thus the shear stress needed for dislocation motion and multiplication to cause plastic deformation is proportional to the elastic shear stress of a deformed material.[11] A compilation on the comparison of Vickers hardness data on the shear moduli and the bulk moduli taken over a thousand measurements clearly shows that the shear modulus of polycrystalline aggregates is a better qualitative predictor of hardness than bulk modulus, Figure 2.7. [11] Thus the prediction of hardness on the bulk modulus value may be misleading owing to the greater scatter of hardness-bulk modulus relationship.

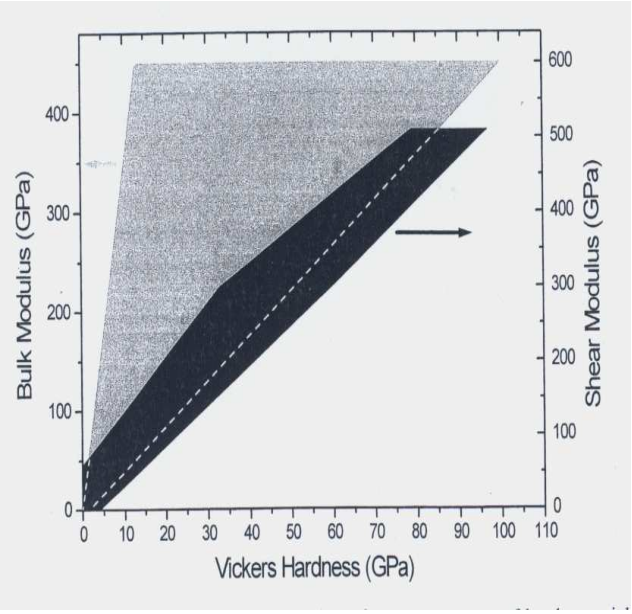

Figure 2.7: The scattering of Vickers hardness for a set of representative hard materials in comparison with bulk modulus (gray region) and shear modulus (black region). [11]

2.5.1.1: Hardness Test Methods

Hardness is normally measured by techniques that scratch or dent the surface.[35] The scratch method is the longest established, Mohs' scale of relative hardness for minerals being well known as an empirical means of ranking.[35] Diamond is ranked 10 on the Mohs' scale and is the hardest known mineral with talc ranked 1 and as the least hard in the list. At present it is more common to use an engineering indentation test, of which there are a number of varieties differing in load applied and geometry of the indenter.[35] All the methods give a measure of the penetration of the indenter into the material. Hardness tests commonly employed for ceramics, as evidenced in manufacturers' brochures and scientific literature, divide into three main types: [35]

i.) Vickers test (diamond square-based pyramid indenter)
ii.) Rockwell Superficial test (diamond ball-ended cone indenter)
iii.) Knoop test (diamond rhombohedral-based pyramid)

There are standard procedures which are based on research and test practice with metals and other more ductile materials for each of the above tests.[34] Hardness measured on one scale is usually different from hardness measured on another ,i.e., hardness is not a physical parameter but a material response to certain conditions of test. Conversion from one scale to another is not recommended.[34]

i.) Vickers test :

This involves the measurement of the diagonals of a residual pyramidal impression after removing a given applied load. The indenter is in the form of a square-based diamond pyramid. There are two main types of tests namely 'macrohardness' test, in which loads in the range 30kg down to 1kg are used and 'microhardness' tests, which are made at loads in the range from 1000g down to 10g.[34] The microhardness tests are carried out on adapted microscopes or specialised derivatives of microscopes.[34]The result of a test is expressed as a Vickers hardness number under a stated load in 'kg' in actual fact it is the force per unit area of the impression given by :[34]

$$HV = \frac{1.8544P}{d^2} \qquad (2.44)$$

where P is the load in kg and d is the mean of the two diagonals in mm.

Macrohardness testing of ceramic materials normally results in considerable cracking which may disguise the corners of the impression.[34] The extent of cracking is related to grain size and fracture toughness and acceptable measurements are feasible below 5kg in most cases.[34] Recommended practice is that a quoted number for a material should be the average from 5-10 randomly positioned macrohardness tests, and preferably more than 20 randomly positioned microhardness tests.[34] This is done owing to the scatter of results normally obtained on ceramics as a result of their multiphase nature, their generally non-

cubic symmetry, and porosity that exists below the surface of the test piece.[34] It is therefore not uncommon to obtain coefficients of variation of 10% in macrohardness measurements and 20% in microhardness measurements.[34]

ii.) Rockwell Superficial test :

This method was originally designed for use on thin metallic components and coatings, but test data on bulk ceramics are often quoted.[34] Rockwell test involves measuring the penetration produced by a major load, less any elastic or recoverable strains. The procedure entails applying a minor load typically 3kg to the indenter, zeroing a displacement scale, applying and removing an additional load and taking the reading when the displacement needle stops moving.[34] Hardness values are quoted according to the relation:[34]

$$HRN = 100\text{-}e \qquad (2.45)$$

where e is the depth of penetration in μm.

It is recommended practice to make at least 5 determinations and quote the mean value and scatter of the results.[34]

iii.) Knoop test :

This method has been used extensively for the study of hard ceramics because the long axis of the indentation is typically 2.5 times that of a Vickers impression at the same load. This makes it more readily measurable than the Vickers.[34] The impression is in the form of a rhombohedral-based diamond pyramid with a major axis which is 7 times the minor axis.[35] The hardness number is calculated using the projected area as opposed to the actual surface area and is given by :[34]

$$HK = \frac{14.229P}{d^2} \qquad (2.46)$$

where d is the length of the long diagonal in mm and P is the load in kg.

2.5.1.2: Factors affecting hardness

The hardness of brittle materials has a strong dependence on the flaws present which act as stress concentration sites incapable of relaxing plastic deformation.[11] These flaws are present in many forms in most hard materials. The most prominent being residual stresses, microstructural textures, grain size, porosity and the structure of grain boundaries.[36] In practice sintered specimens usually have a relative density below 99%.[36] This leaves some residual porosity which has been found to affect the hardness in a negative sense.[36] Pores are less resistant to indent penetration thus they present regions of low hardness in the material. It has been observed that small porosity levels of 1-2% can affect the hardness more than an increase in the grain size from 0.5μm to 2μm.[36] This is illustrated in Figure 2.8 below;

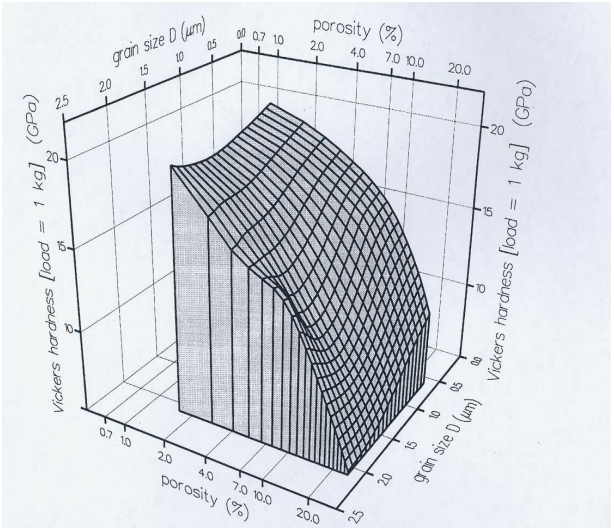

Figure 2.8: Effect of porosity and grain size on the hardness of a typical ceramic material.[36]

It has been observed that any polycrystal exhibits a hardness like the single crystal if the load is small enough ,i.e., if only a few grains are affected.[36] At higher loads the indentation size becomes much larger than the grains and in polycrystals this size effect is partly offset by the hindrance of dislocation activity due to close spacing of grain boundaries, in the case of fine grained microstructures.[36] On the other hand with coarse grained microstructures there is less resistance to plastic deformation because of lower hindrance to dislocation activity. This in itself explains why fine grained materials are found to be harder than their coarse grained counterparts. This is also highlighted in the Hall-Petch relationship below which shows the inverse relationship between the hardness and the grain diameter, d.[36]

$$H = H_0 + \frac{K_0}{\sqrt{d}} \qquad (2.47)$$

where H = hardness of polycrystalline material in GPa, d = mean grain size of randomly oriented grains in μm, H_0 = average hardness of pure crystal, and K_0 = Hall-Petch coefficient.

Hardness has also been found to be affected by the structure of grain boundaries typically in liquid phase sintered materials.[35] Theoretically Si_3N_4 has a Vickers hardness in the region of ~17-18GPa but the liquid phase sintered counterpart has a reduced hardness.[35] This reduction in hardness is thought to be due to lowered resistance to indent penetration by the binder material present at the grain boundaries.

The factors discussed above are all related to the material properties. There are also factors related to the environment such as temperature and moisture present, those related to the equipment used such as geometry of the indent and magnitude of the applied load. Detailed discussions of these factors are dealt with thoroughly in various other publications.[36-37]

2.5.1.3: Fracture Mechanics of ceramic materials

Ceramic components in most cases fail by unstable propagation of cracks initiated at flaws which are present due to manufacture or surface treatment.[37] These flaws are usually in the form of pores, cracks and inclusions. The brittle behaviour of ceramics is attributed to low resistance to crack propagation.[35, 37] There are two main methods used for characterising the crack propagation behaviour of materials. The more commonly used method is the evaluation of the fracture toughness K_{IC}. K_{IC} is a critical value of the stress intensity factor K_I. The latter quantity serves as a scale factor to define the magnitude of the crack tip stress field.[37] K_I is depended on the applied load, initial size of crack and geometry of the component.[37] and has been found to increase until unstable crack propagation occurs at some critical value, i.e., $K_I = K_{IC}$.[38] There are basically 3 loading modes which result in high stresses at the crack tip namely:

i.) Mode 1: tension normal to the crack plane.
ii.) Mode 2: shear loading in crack direction.
iii.) Mode 3: out of plane shear loading.

Mode 1 has been found to be the most important.[38] An alternative method is based on energy considerations in crack propagation described by the crack resistance factor G_{IC}. This idea is referred to as the Griffith criterion.[37-38]

The criterion compares the magnitude of the strain energy released to that consumed by a crack increment, so called R, representing the resistance to cracking.[38] An equilibrium condition occurs when the difference, $G-R = 0$ and crack growth is favoured if $G-R > 0$, and healed when $G-R < 0$ This forms the basis of the Griffith criterion.[38]

It has been observed that the most problematic part of toughness determination is to create a crack and to measure its size.[37] There are several methods in use for fracture toughness determination, detailed discussion of which is presented in a

number of publications.[36-38] In the present work Vickers indentation was used to initiate cracks which were used to determine the fracture toughness of the material. This is a common method used for ceramic materials owing to its versatility and reliability.[34]

2.5.1.4: Vickers indentation cracks

Fracture toughness determination with Vickers hardness indentations was proposed by Evans *et al* [39] and later extended by Niihara *et al* [40] and Anstis *et al* [41]. The fracture toughness is calculated from the length of cracks which develop during a Vickers indentation test and can be measured optically at the specimen surface. [40-41] The basic procedure for fracture toughness determination consists of three main steps namely: [35]

i.) Generation of a crack in a test specimen.
ii.) Measurement of load of failure.
iii.) Calculation of K_{IC} from failure load, failure stress and crack depth using relations depended on crack length, specimen dimensions and yield stress.

The fracture toughness value can be obtained from the relation (2.48) ;

$$K_{IC} = 0.032H\sqrt{a}\left(\frac{E}{H}\right)^{\frac{1}{2}}\left(\frac{c}{a}\right)^{-\frac{3}{2}} \qquad (2.48)$$

H = hardness ,E= Young's Modulus, a = half the indent diagonal, and c = length of crack.[35]

In the development of new ultra hard or composite materials the Young's Modulus value, E is usually unknown. It is common practice to adopt relations independent of E, Shetty *et al* [42] developed a relationship based on the Palmqvist radial cracks found on the specimen surface shown below: [41]

$$K_{IC} = 0.0889\sqrt{\left(\frac{H \times P}{4l}\right)} \qquad (2.49)$$

H = Vicker's hardness, P = indent load, l = c-a where $2a$ = indent diagonal and $2c$ = length of full crack.

The development of cracks in brittle materials occurs in a sequence of steps. Under the indentation load the elastic limits of most ceramic materials are exceeded, a zone of plastic deformation develops beneath the pyramidal indenter.[43] The indenter acts as a wedge and induces tensile stresses in the surrounding material.[41] During the loading phase, these tensile stresses overlap with compressive stresses caused by the applied indentation load. There is development of cracks but with restricted mobility. When the load is removed from the indenter, the compressive stress component ceases to exist, and cracks formed assume their final length.[41] The cracks will grow to a point at which the stress intensity falls below its critical value.[41]

Given the variety of cracking mechanisms associated with ceramic materials, both the stress field under load and the residual stress are clearly very complex.[35] Additionally in materials with large grain size and single crystals irregular cracks and lateral cracks which proceed parallel to the surface causing chipping may develop.[36] The presence of residual stresses in the vicinity of the crack also result in subcritical crack growth in air. All these lead to an underestimation of the fracture toughness value. It is common practice to create indentation cracks in oil to avert subcritical crack growth in air and to measure the crack size immediately after indentation.[36]

2.5.2: Wear of Ceramic materials

Ceramic materials have long been promoted as promising materials for use in tribological applications due to their high hardness, high temperature stability and chemical inertness relative to metals.[44] However their inherently brittle nature creates a concern for potential premature catastrophic failures.[45] Wear of ceramic

materials is highly depended on both operating conditions (normal load, velocity and temperature) and material properties (grain size, mechanical and thermal properties).[46-48] Previous and ongoing studies have shown that wear of ceramics depends to a large extent on the 'wear mode' occurring at the machining onset.[43] At low loads and relatively low temperatures the wear mode is to a large extent controlled by the tribochemical reactions. On the other hand at higher loads and higher temperatures, the dominant wear mode is mechanical wear occurring by propagation of cracks along grain boundaries resulting in micro fracture within the material.[43] In the later case the microstructure of the material is expected to play a more significant role than its chemical stability. [43] This clearly highlights the interlink between the fracture toughness, rapture strength, hot hardness and materials' tribological properties. As highlighted before, hardness alone does not guarantee good wear or tribological properties in any one material. A compilation of the key properties of some representative ceramic cutting tool materials in Figure 2.9 below shows the relationships highlighted above.[36] It is clear that the trend now is towards development of newer materials possessing high toughness and hot hardness which implies good wear properties.

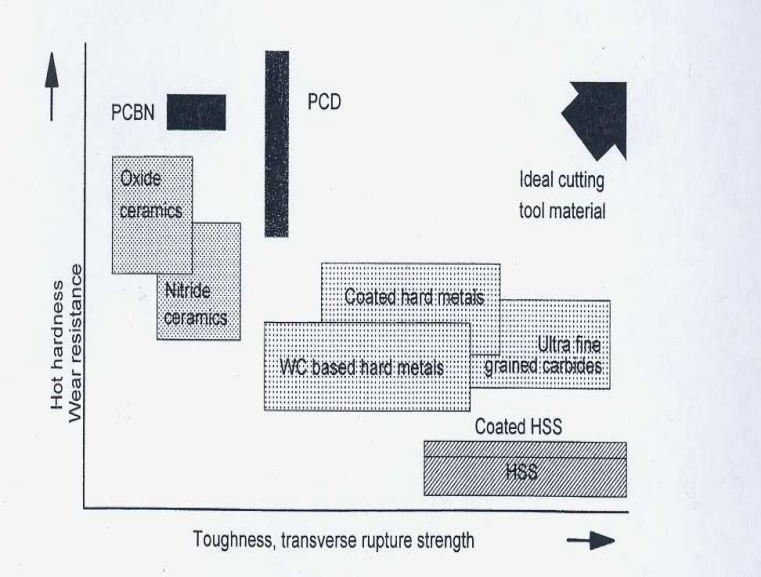

Figure 2.9: Relationship between wear resistance and microstructure related properties.[36]

Chapter 3: Experimental

This section describes the experimental procedures, equipment and chemicals used in the present work. Brief outlines of the equipment functions are given and references are highlighted for the detailed descriptions thereof.

3.1: List of chemicals

Chemical name & purity	Supplier
70wt% Zirconium-propoxide	Sigma-Aldrich
99.99% anhydrous tantalum chloride (25g)	Sigma-Aldrich
Absolute ethanol	Sigma-Aldrich
99.99% UHP ammonia gas	Afrox
99.99% UHP nitrogen gas	Afrox
99.99% UHP oxygen gas	Afrox
99.7% 2-propanol	Saarchem
De-ionised water	Wits Chemistry Dept.

3.2: Equipment used

The following is a list of the equipment used to carry out synthesis and analytical experimental work;.

3.2.1: Planetary mill

A Fritsch pulveressete type planetary mill was used to reduce the particle sizes of the oxide powders. Dry milling of about 15g batches of powder with a ball to solids ratio of ~5:1 was done in a steel milling chamber with 4mm diameter steel balls. The mill was programmed to mill continuously at 250rpm for 4 hours for all the batches. Particle sieving was done after milling of each batch to monitor the efficiency of milling and oversize powders were remilled until the targeted particle size was achieved. Powders were washed in absolute alcohol to remove impurities picked up during milling.

3.2.2: Tube furnace

A horizontal type tube furnace was used for nitridation experiments. This consists of molybdenum disilicide heating elements suspended from the roof of the furnace casing to hang freely along the side walls on the inner side of insulators. Insulation was provided for by high temperature refractory board surrounding the tube. A platinum-rhodium thermocouple positioned in the heating chamber was used as a temperature sensor providing raw data for temperature readings to the programmer. A silica tube 1200mm in length and 40mm external diameter was used as the chamber containment for the flowing gas and sample. The samples were placed in alumina boats in the vicinity of the hot zone (middle section of the chamber). The heating and cooling cycles were programmed through the temperature programmer installed on the furnace.

3.2.2.1: Thermal Nitridation Device

The nitridation device consisted of a horizontal tube furnace with a silica tube reaction chamber of length 1200mm and outside diameter of 40mm with a CNB40 glass connection at one end to facilitate for the sample insertion. The ammonia gas was supplied to the reaction chamber by means of a rubber nylon composite tube. The set-up is illustrated by the diagrams below.

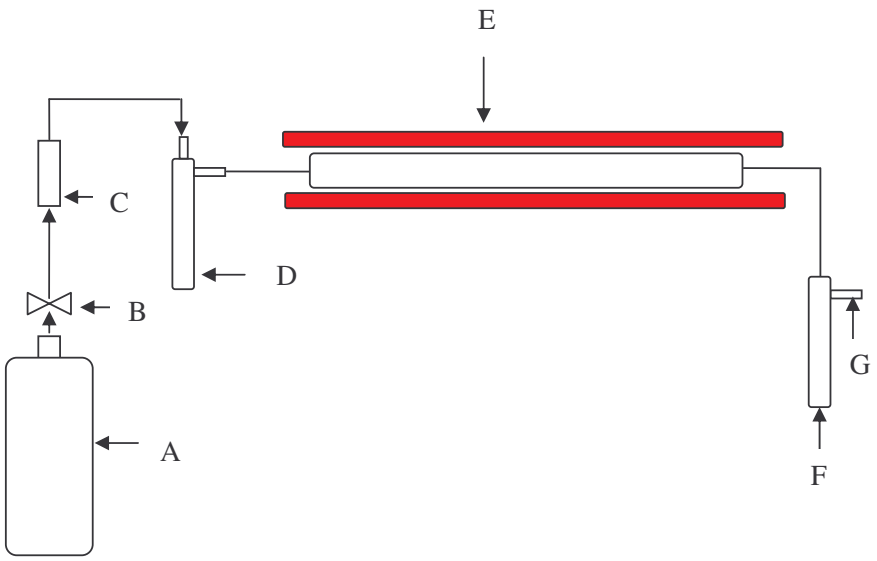

Figure 3.1: Schematic representation of nitridation device

List of components in Figure 3.1:

A: ammonia gas tank.

B: stainless steel regulator valve.

C: flow meter (pyrophylite ball).

D: gas bubbler (water).

E: Silica tube inside tube furnace.

F: gas bubbler (soaking ammonia).

G: gas outlet.

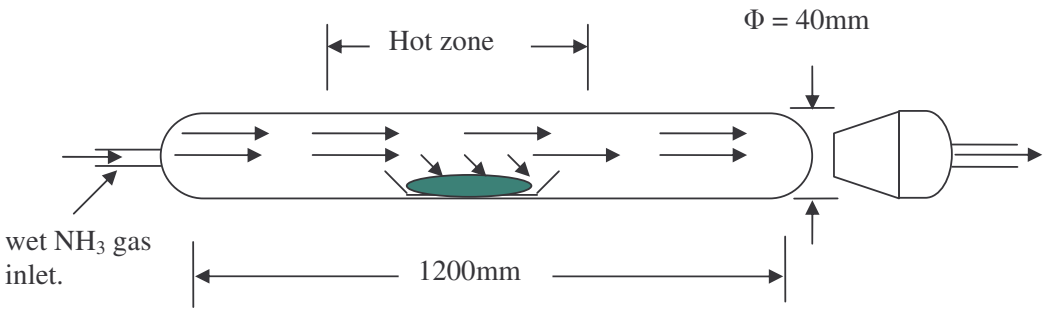

Figure 3.2: Exploded view of reaction chamber (silica tube) used for nitridation.

3.2.3:X-ray diffraction

The phase composition was determined by X-ray diffraction, using a Philips X-ray machine equipped with a PW1830 diffractometer with CuKα irradiation operated at 40kV and 20mA. All measurements were taken using a step scan of 0.020^0 recorded in the 2θ range of $10\text{-}80^0$ for 1hour and 30minutes. Patterns were collected with the aid of APD powder diffraction software and phase identification was done using X'Pert HighScore software containing ICDD (International Centre for Diffraction Data) data files for comparison. The tantalum oxynitride patterns were compared with pattern JCPDS card # 70-1193 and the TaZrON phases were compared with JCPDS card # 49-1521.

3.2.4: Hot Press

Variable temperature sintering experiments were carried out in a high temperature furnace with a hydraulic mechanical pressing mechanism (hot press). The hot press is essentially a high temperature furnace ($T \leq 2100^0C$) which consist of a graphite heating element suspended from the roof to hang freely along the walls

covering the whole die length. A pyrometer window situated adjacent to the chamber is used as a temperature sensor providing raw data to the temperature programmer on the control panel. Vacuum was maintained in the chamber by means of a vacuum pump which can maintain a vacuum of 10mtorr (~$1.33*10^{-3}$ bar). The chamber is sealed from the outside environment by means of rubber 'o' rings held in place with high pressure vacuum grease. A gas flow is maintained in the chamber by means of a gas supply cylinder equipped with a suitable flow meter. Mechanical pressing of the sample in the crucible was achieved by means of graphite punches. The maximum attainable pressing load is determined by the external steel loading frame and the graphite die set used. The external steel loading frame can sustain a load up to 10 000kg and for a 24mm internal diameter graphite die only up to 3000kg (~66MPa of pressure on the sample) of load are permissible. The temperature profiles were programmed using the temperature programmer on the control panel and pressing load was applied by adjusting the appropriate knobs on the control panel.

3.2.5: Particle size analyser

A Mastersizer 2000 was used for particle size analysis. This utilises Fraunhofer diffraction of light formed by particles with a diameter larger than the incident laser beam wavelength. A combination of an optical filter, lens, and photodetector coupled with a computer with Mastersizer software enabled computation of the particle size distribution from the diffraction data. The samples were prepared in an ammonium polyacrylate deflocculant at ~ pH8.30 and delivered to the optical unit using a water medium (dispersant). The Mastersizer 2000 was then used to capture the scattering pattern from the prepared sample which was then displayed and stored as volume% against the particle size. All measurements were done using an obscuration of >10%.

3.2.6: Oxygen and Nitrogen analyser

An ELTRA 2000 ONH analyser which uses a combustion method was used to estimate the amount of oxygen in the sample, a standard copper sample containing ~0.1wt% oxygen was used for standardisation. The amount of oxygen was estimated from an average of three readings collected using Proton software. The amount of nitrogen was estimated from the weight change data after oxidising samples in air.

3.2.7: Thermo gravimetric analyser (TGA)

Thermo gravimetric analysis was used to determine the thermal stability of the sol-gel produced powder in air and the nitrided powder in nitrogen and air. This was achieved by monitoring the %weight change with increasing temperature up to 1000^0C. This was done on a Perkin Elmer TGA 1 using Pt sample cups under constant gas flows. A platinum rhodium thermocouple situated close to the sample was used for temperature readings. The equipment is coupled with a microcomputer with suitable software for data analyses and storage.

3.2.8: Scanning electron microscope

A Philips XL-30 SEM (scanning electron microscope) connected to a microcomputer with suitable software which was used for microstructural analysis of the sintered samples. Sample preparation was carried out in accordance with the conventional solid sample materialographic preparation methods. The samples were coated with a thin layer of gold for about 60 seconds and mounted on aluminium studs with the aid of a carbon tape. Secondary electrons were used to take images at a voltage of 10.0kV and a magnification range of 1000x-20000x at various spots. Energy dispersive spectroscopy (EDS) was used for elemental analysis.

3.2.9: Image analyser

The image analyser in principle is an optical microscope connected to a microcomputer with suitable software. This tool was used for the analyses of polished samples and estimation of microcracks lengths used for fracture toughness measurements. The surfaces of samples were monitored to ensure complete removal of surface scratches at each grinding and polishing stage. Indentation cracks formed during hardness testing were measured using AxioVision software which was used to calculate the fracture toughness values for the high pressure sintered samples.

3.2.10: Hardness tester

A Vickers hardness tester was used for all the hardness measurements. This essentially consists of a diamond indenter in the form of a pyramid with a square base and an angle of 136^0 between opposite faces. A load of 5kg was applied for 10seconds for each sample and readings taken from the scale provided on the machine. Conversion tables were used to obtain the Vickers' hardness numbers which were in turn converted to hardness values in GPa.

3.3: Preparation of oxide gels

A sol-gel process was used to obtain active oxide precursors containing both tantalum and zirconium and tantalum only according to the flowchart (Figure 3.3). $TaCl_5$ *(Aldrich)* and zirconium propoxide *(Aldrich)* were used as the starting materials. A mixture of 25grams $TaCl_5$ and calculated amounts of 70wt% solution of zirconium propoxide were added to 100ml beakers and sealed with parafilm. The mass of $TaCl_5$ was fixed in all cases. Calibrated amounts of absolute ethanol *(Aldrich)* were added to each beaker and solutions continuously stirred for about 15 minutes with a magnetic stirrer ensuring dissolution of all the $TaCl_5$. These experiments were carried out in a fume box until the cessation of HCl fumes. The mixtures were hydrolysed with deionised water by a drop wise injection method (approximately one drop/second) with continuous stirring at room temperature to a thick sol. The mixtures were kept at 80^0C for 24 hours. Gels were obtained within the specified period. The gels were oven dried at 100^0C for 12 hours. Thermogravimetric analyses of the dried gels were done to obtain the calcining temperatures. The gels were dry milled for 4 hours in a planetary mill using 4mm diameter zirconia milling balls at a speed of 250rpm. The powders were washed with absolute ethanol to remove the impurities introduced during milling. The powders were calcined at 600^0C for 6hours in the case of Ta_2O_5 and 700^0C in the case of Ta-Zr oxide gels.

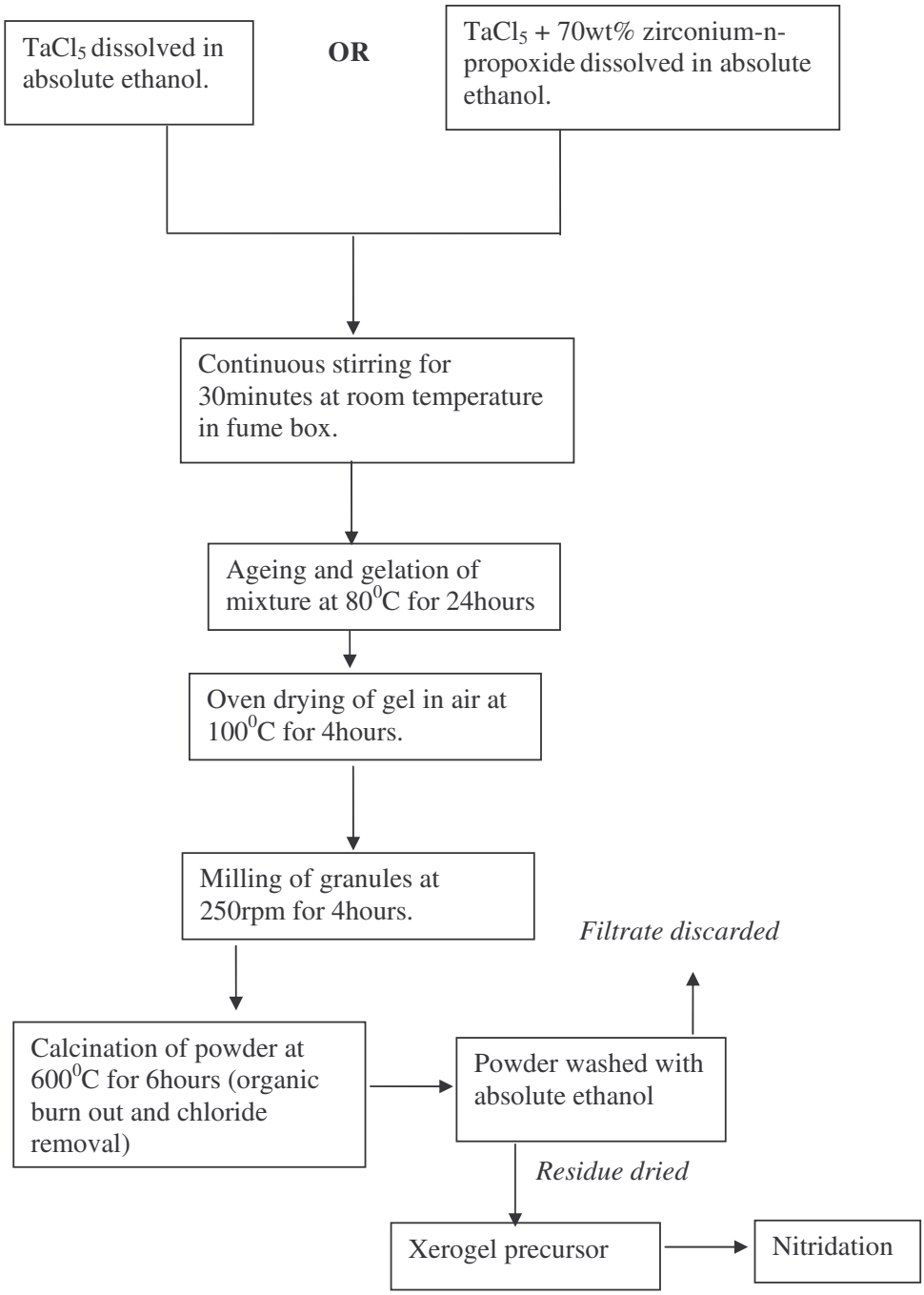

Figure 3.3: Flowchart for the sol-gel synthesis of oxide precursor powders and subsequent nitridation to oxynitride.

3.3.1: Mass requirements

The mass requirements for the sol-gel produced oxides were determined in accordance with the procedure by Guenther *et al*.[5] The mass of the $TaCl_5$ used was fixed at 25g and other additions to be made were calculated using balanced stoichiometric equations.

Mass requirements for Ta_2O_5 synthesis

The dissolution reaction was used to calculate the amount of absolute ethanol required to dissolve $TaCl_5$ stoichiometrically. To ensure complete dissolution about 50% excess absolute ethanol was used in all batches.

Dissolution reaction:

$$TaCl_5 + 5C_2H_5OH = Ta(OC_2H_5)_5 + 5HCl \qquad (3.1)$$

The amount of water added for the hydrolysis reaction corresponded to twice the amount of alkoxide present in the mixture Table 3.1. In this calculation it was assumed that with the amount of water used the hydrolysis reaction would go to near completion through the reaction below. The water to alkoxide ratio used R=2 is close to the value required for water condensation reaction 2.9 to be favoured ($R \geq 2.28$) as discussed in Chapter 2.

The hydrolysis reaction was predicted to proceed as in reaction 3.2 below;

$$Ta(OC_2H_5)_5 + H_2O = Ta(OH)(OC_2H_5)_4 + C_2H_5OH \qquad (3.2)$$

In this case there is complete substitution of the alkyl group $-OC_2H_5$ by the hydroxyl group $-OH$.

Mass requirements for the $Zr_xTa_{1-x}O_{2.75-x}$

The mass requirements for the mixed oxides were calculated from the atomic ratios of the targeted phases chemical formulae. The mass of $TaCl_5$ was fixed at 25g in all three cases. The mass requirements for the absolute ethanol required to dissolve $TaCl_5$ were calculated as per procedure above. From the ZrO_2-Ta_2O_5 phase diagram, Figure 2.3, complete solid solubility is attainable in the regions approximately equivalent to 14.3-33% Ta_2O_5 and >80% Ta_2O_5. A composition of 50% Ta_2O_5 was also prepared to confirm the validity of the phase diagram. The aim of the experiments was to obtain solid solutions of tantalum and zirconium oxides. An alkoxide 70wt% solution of zirconium propoxide (*Sigma-Aldrich*) was used as the source material for zirconium ions. The mass of 70wt% solution of zirconium propoxide (M_{ZP}) was calculated as below;

$$M_{ZP} = \frac{M_P}{0.7} \qquad (3.3)$$

where M_P is the mass of zirconium propoxide (in grams) present which was obtained from equation 3.4 below:

$$M_P = \left(\frac{m_{TaCl_5}}{R_{TZ}} \right) RMM_{ZP} \qquad (3.4)$$

m_{TaCl5} is the moles of $TaCl_5$ present in 25g and R_{TZ} is the ratio of moles (no units) of tantalum to zirconium present in the targeted chemical formula and RMM_{ZP} is the relative molecular weight of zirconium propoxide (in g/mol). The quantities used for all the four experiments are summarised in Table 3.1 below:

x	$TaCl_5$/g	70wt%$Zr(OPr)_4$/g	$Zr(OPr)_4$/g	H_2O/ml	Target phase
0.00	25.00	0.000	0.000	56.7	Ta_2O_5
0.33	25.00	66.237	53.286	189.13	$Ta_{0.30}Zr_{0.70}O_{2.42}$
0.50	25.00	32.624	22.837	121.91	$Ta_{0.5}Zr_{0.5}O_{2.25}$
0.80	25.00	8.156	5.709	72.97	$Ta_{0.8}Zr_{0.2}O_{1.95}$

N.B: amount of absolute ethanol used corresponded to 30.6ml in all cases.

Table 3.1: Composition of starting mixtures for the preparation of oxide gel precursors.

The mixtures were allowed to undergo condensation in all cases followed by ageing for 24 hours at 80^0C maintained in a paraffin bath using a hot plate as the heat source. This allowed for the formation of oxide networks with subsequent formation of excess water after condensation reactions. This is in accordance with the discussion in Chapter 2 on sol-gel synthesis of oxides, where the water condensation dominates when the water to alkoxide ratio corresponds to R≥2.28. In the present work R=2. This also favours the water condensation reaction but to a lesser extent. In both cases there is formation of the oxide network as highlighted below;

Water condensation reaction:

$$2Ta(OH)(OC_2H_5)_4 = 2(C_2H_5O)_4 - Ta - O - Ta - (OC_2H_5)_4 + H_2O \quad (3.5)$$

Alcohol condensation reaction:

$$Ta(OC_2H_5)_5 + Ta(OC_2H_5)_4(OH) = (C_2H_5O)_4 - Ta - O - Ta - (OC_2H_5)_4 + C_2H_5OH \quad (3.6)$$

In the case of the mixed oxide, i.e, introduced by the addition of zirconium propoxide, the water condensation reaction would proceed in the same manner resulting in cross linking of tantalum and zirconium ions in the same network as shown below.

$$2(C_2H_5O)_4(C_3H_7O)_3 - Ta - Zr - O - Ta - Zr - (C_2H_5O)_4(C_3H_7O)_3 + 2H_2O \quad (3.7)$$

Clearly from the condensation reactions there is still some alkyl group and chloride impurity present in the oxide matrix. The oxide gels were subsequently dried in air in an oven at 100^0C for 4hours. The dried gels were milled using 4mm steel balls in a planetary mill at 250rpm for 4 hours. The resulting powders were calcined to different final temperatures (600^0C in the case of the Ta_2O_5 powder and 750^0C for the Ta-Zr oxide gels) in a muffle furnace for 6 hours at a heating and cooling rate of 10^0C/min to get rid of the alkyl group impurities present. The powders were washed with excess absolute ethanol to remove impurities picked up during milling and any residual chloride ions present.

3.4: Oxide powder characterisation

In order to assess the quality of the sol-gel produced oxide precursors, analyses on the particle size, phase composition, thermal stability, X-ray diffraction and surface area were done. The powders were analysed by Energy Dispersive Spectroscopy (EDS) in scanning electron microscopy (SEM) for residual chloride. The average particle size was measured using a Malvern analyser *(Mastersizer 2000)* with Mastersizer 2000 analysis software. Scanning electron microscopy was used to visualise the morphology and to determine the size of the powder particles. X-ray diffraction was used for phase analysis. The thermal degradation / stability of the uncalcined gels were measured using a thermogravimetric analyser at a rate of 10^0C/min up to a maximum temperature of 1000^0C. Surface area measurements were done using the BET method. The results obtained were used to predict the conditions and feasibility of the subsequent nitridation process. For instance nitridation is mostly efficient with fine and high surface area of powder particles in order to be able to catalyse the ammonia decomposition reaction. Thus fine powders are preferred in this instance.

3.5: Thermal Nitridation

In order to obtain the oxynitride phases the oxide precursors were thermally nitrided in flowing ammonia at various ammonia flow rates, ammonolysis times and to different final temperatures in a tube furnace with a silica type tube as the reaction chamber. The reaction chamber consisted a silica tube of length 1200mm and external diameter of 32mm placed in a horizontal tube furnace. Gas connections to the tube were provided by glass fittings. Approximately 2grams of powder was place in an alumina boat for each run. Nitridations were carried out with ammonia gas flow of 20-50cm^3/min in the temperature range of 700-900^{0}C for a time range of 1-12hours. A theoretical compilation of nitridation parameters from previous experiments of a similar nature was used as a guide to predict the most appropriate operating parameters. Table 3.2 shows a summary of the parameters previously used by other researchers.

Starting phase	temp.(^{0}C)	time(h)	Flow-rate (cm^3/min)	Flow conditions	Final phases	Ref.
Ta_2O_5	797	3	100	dry NH_3	Ta_3N_5	[20]
Ta_2O_5	700	40	166.7	wet NH_3	Ta_2O_5	[4]
Ta_2O_5	800	5	166.7	wet NH_3	Ta_2O_5,TaON	[4]
Ta_2O_5	800	10	166.7	wet NH_3	TaON	[4]
Ta_2O_5	800	10	50	wet NH_3	Ta_2O_5	[4]
Ta_2O_5	800	-	-	wet NH_3	TaON	[49]
$Ta_xZr_{1-x}O_{2.75-x}$	>950	36	varied	dry NH_3	$Ta_xZr_{1-x}ON$	[19]
$Ta_xZr_{1-x}O_{2.75-x}$	700	12	10-20	dry NH_3	TaON,Ta_3N_5	[3]
$Ta_xZr_{1-x}O_{2.75-x}$	800	12	10-20	dry NH_3	TaON,Ta_3N_5	[3]
$Ta_xZr_{1-x}O_{2.75-x}$	900	12	10-20	dry NH_3	TaON,Ta_3N_5	[3]
$Ta_xZr_{1-x}O_{2.75-x}$	1000	12	10-20	dry NH_3	TaON,Ta_3N_5	[3]
Fe-Ta_2O_5	900	16.7	160	dry NH_3	TaON,Ta_3N_5	[50]
Fe-Ta_2O_5	900	5mins	160	dry NH_3	Ta_2O_5,Ta_3N_5	[50]

Table 3.2: The dependence of nitridation reaction on time, flow rate, ammonia conditions and temperature.

The table above clearly highlights the interdependency of the parameters in attaining the oxynitride phase. There is a general trend towards oxynitride formation at temperatures above 700^{0}C. This is in agreement with the fact highlighted earlier in Chapter 2 that ammonia gas decomposes at 827^{0}C which in turn provides the higher nitrogen pressure which enables nitridation at relatively low temperatures and atmospheric pressure. Another trend to note is the reproducibility of oxynitride formation under wet ammonia conditions. This has been discussed in greater detail in Chapter 2. This is due to the low energy requirements for the formation of TaON which can easily be surpassed to form the fully nitrided phase Ta_3N_5. The nitridation time is also important but has shown to have a more pronounced effect at higher flow rates. It can be concluded that it is possible to obtain the oxynitride phase provided the nitridation

temperature is high enough to initiate ammonia decomposition, the flow rate is low enough not to favour formation of the fully nitrided phases and the reactions are carried out under wet ammonia conditions.[12] Under these conditions it is presumed that the nitridation time can be kept as low as possible.

Preliminary nitridation experiments were carried out in dry flowing ammonia supplied directly to the furnace without further treatment. These experiments were done to confirm the validity of claims made earlier by other researchers. [3, 19-20, 50]The temperature was raised in the 700^0C to 900^0C range with a heating rate of 20^0C/min. This was done for various nitridation periods (1-12hours) and ammonia gas flow rates of 20-50cm^3/min. The furnace was switched off and powders were allowed to cool to room temperature under flowing ammonia. Owing to the irreproducibility of the preliminary experiments further considerations of tantalum oxynitride thermodynamic data was used to modify the experiments. A second set of experiments were carried out in flowing ammonia using the same parameters of flow rate and temperature as above but in the presence of water vapour. This was achieved by bubbling ammonia through a water bath prior to nitridation. This is in accordance with thermodynamic data compiled by other researchers in previous work of a similar nature.[2,17] The use of water vapour is justified by the low energy requirements for the tantalum oxynitride formation compared to that for the formation of tantalum nitride.[2,17]

3.5.1: Thermodynamic Consideration

TaON thermodynamic data at 298K compiled below explains the justification of using wet ammonia during nitridation.

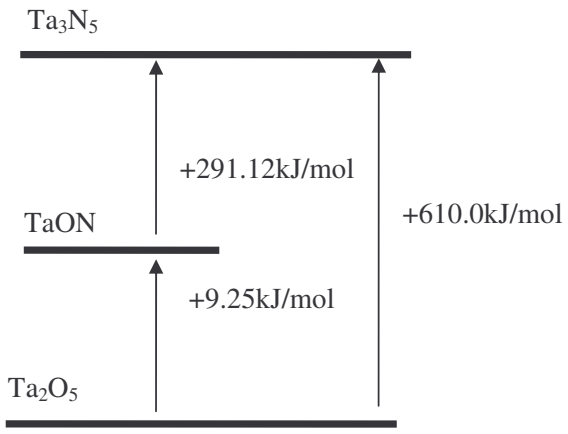

Figure 3.4: The standard enthalpies of reaction between Ta_2O_5, TaON and Ta_3N_5 under ammonia at 298K.[20]

At the onset of nitridation there is more than enough energy to pass the tantalum oxynitride formation stage. The reaction can be said to be controlled by kinetics and under dry ammonia conditions TaON will form in a mixture with either Ta_3N_5 or Ta_2O_5. However the use of water vapour sets up an equilibrium between the nitridation and the opposite hydrolysis reaction. By taking this into consideration the experiments done in the presence of water vapour were highly reproducible. In order to find the effect of flow rate, nitridation time and temperature on the extent of ammonolysis, experiments were done where these parameters were varied. In order to minimise the number of runs the experiments were carried out in the order flow rate, temperature and lastly nitridation time. The flow rate and temperature experiments were done in a period of 4 hours, followed by nitridation time experiments at fixed temperatures and flow rates determined in the previous experiments.

3.5.2: Flow rate experiments

The rate of ammonia dissociation α is a function of the speed of ammonia flow (equation 2.23). In general the fully nitrided phase Ta_3N_5 has been found to be the more dominant phase at high ammonia flow rates.[3] Thus there is need to ascertain the flow rate range most suitable for obtaining the tantalum oxynitride phase. Thermal nitridations were carried out at various flow rates (20-50cm^3/min) at constant nitridation times and temperatures. The samples were analysed by visual inspection and x-ray diffraction.

3.5.3: Variable Temperature experiments

In order to obtain the most appropriate temperature profile for the ammonolysis nitridations were carried out in the temperature range 700^0C to 900^0C. This was done at varying flow rates and constant nitridation times. The samples were analysed for phases present with x-ray diffraction and by visual inspection.

3.5.4: Nitridation time experiments

The time of ammonolysis determines the amount of nitrogen substituting for the oxygen in the oxide precursor. Thermal nitridations were carried out at various times at constant ammonia flow rates and temperature. The analyses were done using a time range of 30minutes to 900minutes at 900^0C in ammonia flow rate range of 20-50cm^3/min.The powders were analysed for phases present by x-ray diffraction and for amount of oxygen and nitrogen present using an ELTRA 2000 ONH Analyser with Proton software for data acquisition and interpretation.

3.5.5: Characterisation of oxynitride powder

The quality of the oxynitride powders obtained was assessed by various methods. Specific powder characteristics were analysed which include particle size,

chemical analyses, X-ray diffraction, surface area and thermal stability in various atmospheres by TGA method. Particle size analyses were carried out using a Malvern Mastersizer 2000 with Mastersizer software for data analysis. This was done in the presence of ultrasonic sound applied for 3 minutes. Chemical analyses were carried out to quantify the oxygen and nitrogen contents by a combustion method using an ONH analyser with Proton software for data interpretation. The heavier metal contents, Zirconium and Tantalum were analysed by Energy Dispersive Spectroscopy (EDS) using a Philips Scanning Electron Microscope. The phase composition of the powders was determined by X-ray diffraction spectroscopy with a Philips PW1830 diffractometer with CuKα irradiation in the 2θ regime of 10-80^0(a step scan of 0.020^0). Surface area determinations were done by the BET method using a Perkin Elmer BET machine. Thermal stability of oxynitride powders in oxidising atmosphere were investigated using a thermogravimetric analyser. This was done at a heating rate of 10^{0}C/min up to a temperature of 1000^{0}C. Additionally thermal stability determinations were done in a nitrogen atmosphere in the temperature range of 1100^{0}C to 1400^{0}C and a heating rate of 10^{0}C/min in a tube furnace. The tube was flushed with nitrogen for 1 hour then heated up to the final temperature and maintained at the final temperature for 1 hour then cooled to room temperature in flowing nitrogen. The mass changes and XRD measurements were done for each run to assess the change in weight and phase purity respectively.

3.6: Hot Pressing

The powders were sintered in the temperature regime of 900^{0}C to 1400^{0}C at a heating and cooling rate of 50^{0}C/min with a dwelling period of 1 hour at pressures of 50-85MPa.This was carried out in nitrogen and inert atmospheres using graphite and h-BN crucibles in an uniaxial hot press. The procedure followed in these experiments is outlined below;

3.6.1: Procedure

i.) Powder pressed into a pellet at 10MPa with a cold isostatic press for 1minute and the green density determined.

ii.) Pellet enclosed in a suitable crucible and outgassed at 600^0C in vacuum (~10mTorr of vacuum) for 30minutes in a hot press.

iii.) Sample heated to a temperature 100^0C below the target temperature at a rate of 50^0C/min under argon atmosphere, followed by dwelling for 15minutes while increasing the pressure up to the target pressure value.

iv.) Temperature increased to the final target temperature at 50^0C/min.

v.) Dwelling at the final temperature and pressure for 1hour while monitoring changes in displacement.

vi.) Cooling down to room temperature at 50^0C/min under argon atmosphere.

The sintered samples were characterised in terms of densification by the Archimedes method and phase purity by X-ray diffraction.

3.7: High Pressure Sintering

An investigation was carried out if the higher symmetry phases can be obtained under pressures of $\leq$5.5GPa starting with pure TaON (x=0) and with smaller amounts of Zr in the system (x=0.7 and x=0.2). TaON powders were hand compacted to green pellets and encapsulated in 17mm Ta alloy cups, outgassed and sealed at 715^0C in vacuum. The powders were sintered under vacuum using a belt type high pressure apparatus in the temperature range 920-1200^0C in a pressure regime of 3-5.5GPa for periods of up to 30minutes. The procedure below was used for sample preparation and sintering.

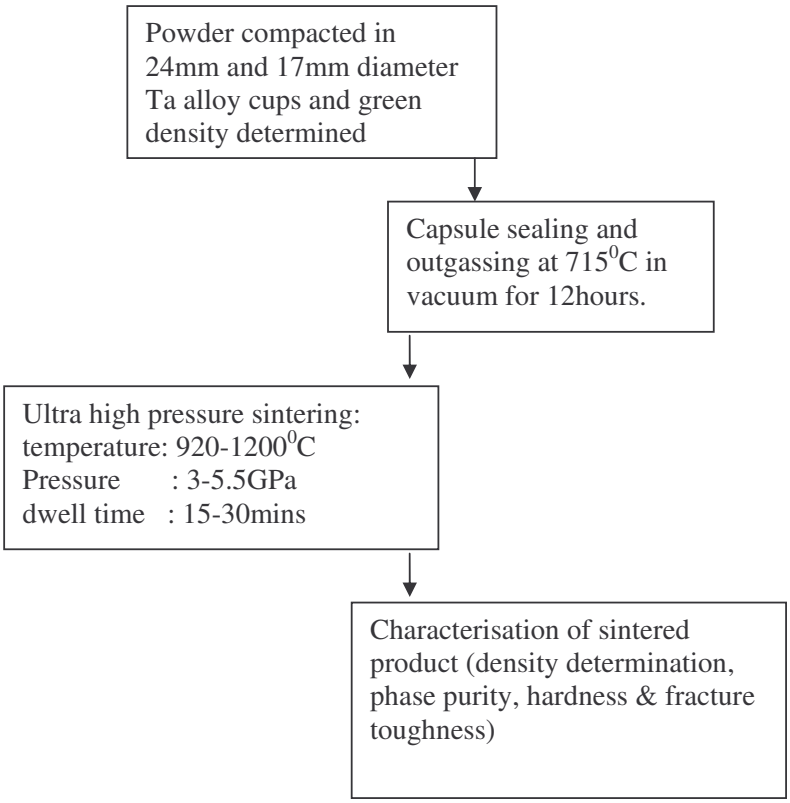

Figure 3.5: Sample preparation and ultrahigh pressure sintering procedure.

3.7.1: Property evaluation of densified materials

In order to evaluate the properties attained after ultra high pressure sintering, the sintered samples underwent a series of procedures to determine the % porosity, hardness, microstructural evaluation, phase purity and fracture toughness. This was achieved using standard procedures for hard materials property evaluation.

3.7.2: Density determination

The sintered density was determined by the standard Archimedes' method. The Archimedes' method consisted of the following steps;

Archimedes' method for density determination:

i.) Specimen cleaned using isopropanol followed by drying in air at 80^0C for 10minutes. The dry weight of the sample *(W_1)* was determined using a balance with an accuracy of 0.1mg (used for all the weight measurements).

ii.) Specimen was boiled in distilled water for 3hours.

iii.) The suspended weight of the specimen *(W_2)* was determined.

iv.) The surface moisture was removed by a light wipe with a damp cloth and the wet weight *(W_3)* determined.

v.) The procedure was repeated to check consistency of weighing.

The open porosity and bulk densities were determined using the calculations below;

$$\text{True volume of the specimen} = \frac{W_1 - W_2}{\rho_w} \tag{3.8}$$

$$\text{True density of the specimen} = \frac{W_1 \rho_w}{W_1 - W_2} \tag{3.9}$$

$$\text{Volume of open porosity} = \frac{W_3 - W_1}{\rho_w} \tag{3.10}$$

$$\text{Bulk volume = volume of specimen + open porosity} = \frac{W_3 - W_2}{\rho_w} \tag{3.11}$$

$$\text{Bulk density} = \frac{W_1 \rho_w}{W_3 - W_2} \tag{3.12}$$

$$\text{volume fraction of open porosity} = \frac{W_3 - W_1}{W_3 - W_2} \tag{3.13}$$

ρ_w denote the density of water in all cases.

3.7.3: Materialographic preparation

Sample preparation for subsequent analyses, i.e., (hardness measurements and fracture toughness determination) was carried out in a similar procedure to that for metal samples. Samples were mounted in a lucite thermoplastic under pressure and a temperature of 150^0C for 15minutes followed by subsequent cooling with water. The samples were mechanically ground with successively decreasing grit of SiC paper (320,500, 1000, 1200 mesh) in the presence of water lubricant at 250rpm. Optical microscopy was used to monitor the progress of grinding at each stage. To ensure grinding marks were completely removed, the samples were rotated 90degrees at each grinding stage. This was followed by polishing with diamond paste (3μm down to 1μm) to a mirror surface.

3.7.4: Hardness Testing

Macrohardness measurements were carried out on the ultra high pressure sintered samples in order to determine their hardness values. Representative samples of approximately 3.0mm in thickness by 4.0mm in length by 3.0mm in width were used for these investigations. The surfaces of the samples were flattened using the materialographic preparation method described previously (see paragraph above). Measurements were done with a 5kg load on 5 randomly positioned spots using Vickers hardness testing method. The load was impressed for 10s using a diamond square based indenter. The diagonals produced were measured and the results of which were expressed as a Vickers hardness number, *HV* obtained from standard Vickers hardness tables which use the formula below;

$$HV = \frac{1.8544P}{d^2} \qquad (3.14)$$

P is the applied load in kg and *d* is the mean of the diagonals formed by the indenter in mm.

The Vickers hardness numbers were converted to hardness values in GPa using the formula below. This is now the more widely accepted way of quoting hardness values in materials engineering.[35]

$$H(GPa) = 0.009807HV \qquad (3.15)$$

H is the hardness value in GPa and HV is the Vickers hardness number.

The quoted values were thus average values taken over five randomly positioned spots. This was done to compensate for the scatter of results normally obtained for ceramic materials as discussed in Chapter 2.

3.7.5: Fracture Toughness determination

Vickers hardness cracks were used to predict the fracture toughness values of the sintered samples. This was done by measuring the length of cracks obtained during indentation using an optical microscope at 20x magnification equipped with AxioVision Software. As previously discussed, fracture toughness determinations for potentially new ultrahard materials are not an easy task owing to the unknown Young's modulus value, E which is very useful in the determination of fracture toughness. However Shetty *et al* [42] developed an equation which can be used in cases were the Young's modulus value is not known. This equation depends on Palmqvist radial cracks found on the specimen surface shown below;

$$K_{IC} = 0.0889\sqrt{\left(\frac{H \times P}{4l}\right)} \qquad (3.16)$$

H = Vickers hardness, P = indent load, l = c-a where $2a$ = indent diagonal and $2c$ = length of full crack.

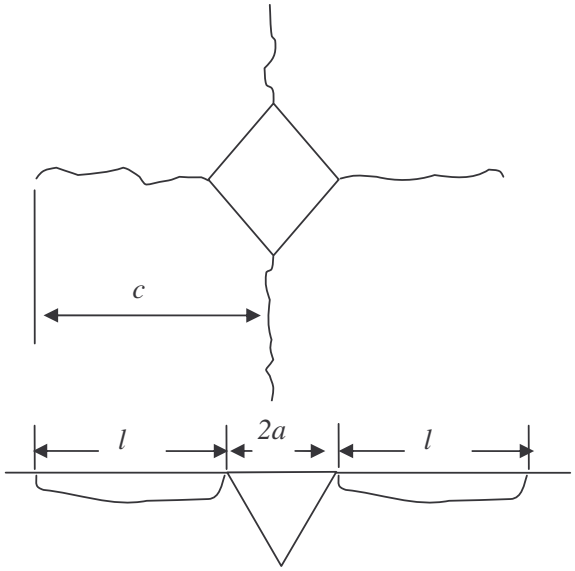

Figure 3.6: Surface cracks morphology and dimensions used to determine the fracture toughness values.

CHAPTER 4: RESULTS AND DISCUSSION

This section covers the overall results of the experiments carried out as described in Chapter 3. This encompasses the characteristics of the oxide powder produced, thermal nitridation results, variable temperature sintering, ultra high pressure sintering results and evaluation of mechanical properties.

4.1: Characterisation of Zr_xTa_{1-x}-Oxide powders

The powders obtained by sol-gel as in the procedure described in Chapter 3 were characterised in terms of thermal degradation by thermogravimetric analysis (TGA), particle morphology by SEM, surface area by the BET method and elemental analysis by EDS in SEM. X-ray diffraction results show that all the gels obtained by sol-gel were amorphous.

4.1.2: Thermal stability of Ta-Zr gels

An investigation on the thermal stability of the oxide was carried out to assess the efficiency of alkyls and chloride ions removal from the oxide matrix. EDX results of the Ta_2O_5 show some chloride ions in the mixture as shown in Figure 4.1 and 4.2 below.

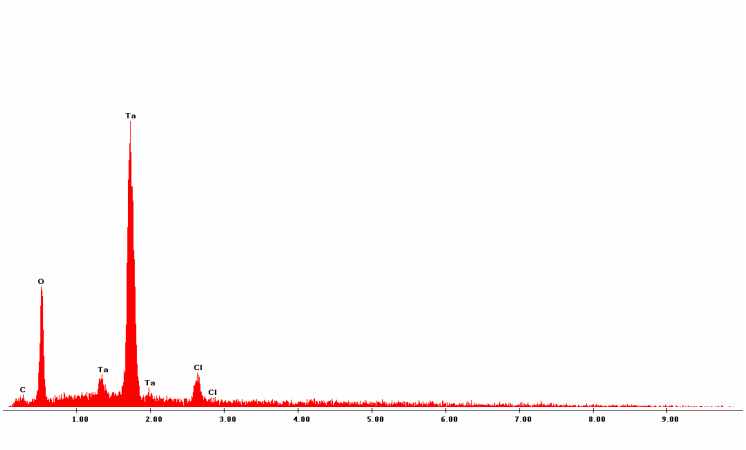

Figure 4.1: EDX results of Ta_2O_5 showing some Cl^- ion impurity after heat treatment at 600^0C for 6hrs.

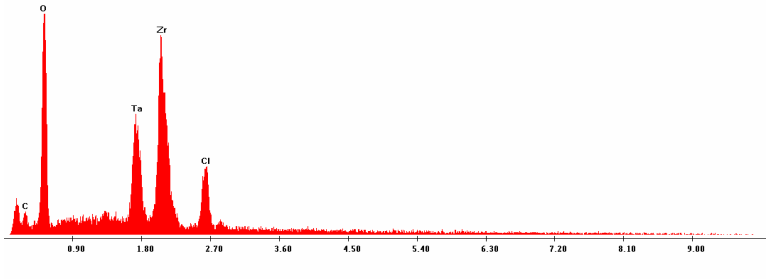

Figure 4.2: EDX results of $Ta_{0.3}Zr_{0.7}$ oxide showing some Cl^- ion impurity after heat treatment at 700^0C for 6hrs.

Typical thermogravimetry curves for the Ta-Zr gels are shown in Figure 4.3 below.

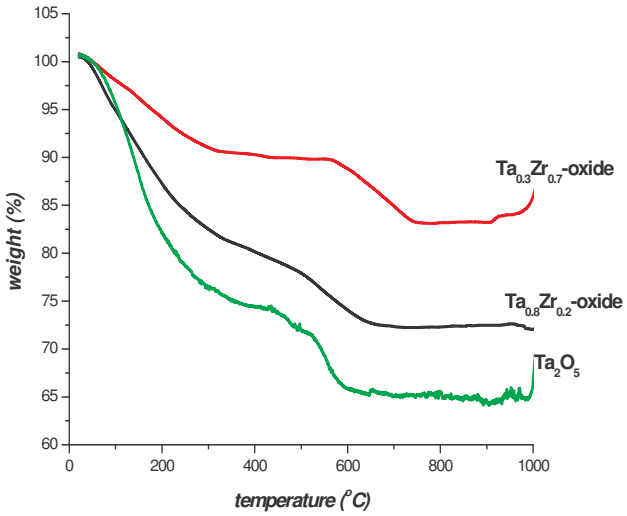

Figure 4.3: Thermal stability curves for the decomposition of Ta-Zr gels in air up to 1000^0C at 10^0C/min.

A maximum weight loss of 34.11% was recorded for the Ta_2O_5 gel using an average of 35mg of sample weight. The weight change was found to occur at

~591.8^{0}C. Weight losses of 27.4% and 16.65% were recorded for the $Ta_{0.3}Zr_{0.7}$-oxide and $Ta_{0.8}Zr_{0.2}$-oxide respectively using approximately the same masses. The respective transition temperatures were found to be ~664.6^{0}C and ~750.8^{0}C. Previous studies by Grins *et al* [2] show lower weight losses of up to ~20% with a decomposition temperature of ~800^{0}C for gels synthesised under acidic conditions and ~55% at ~500^{0}C for gels synthesised under basic conditions with a nominal formula $Ta_{1-x}Zr_xO_{1+x}N_{1-x}$ (x=0.18 and 0.68 under acidic and x=0.80 and 0.13 under basic conditions). In the present work hydrolysis was carried out under neutral conditions hence the values obtained for the decomposition temperatures and weight losses lie in between the two extremes. However the weight loses do not follow a specific trend. The decomposition temperatures obtained above were used as calcinations temperatures of the gels inorder to drive off the alkyl and chloride impurities incorporated during synthesis.

4.1.3: Particle size analysis of the oxide phases

Particle sizes of the oxide gels were found to be in the submicron range (~0.5-2μm) in all cases as shown in Figures 4.4 & 4.5 below. The SEM micrographs show high surface area and fine morphology as expected for sol-gel produced powders. Agglomerates of ~0.1μm have been reported elsewhere using the same synthesis method but under basic conditions. [2] Gels hydrolysed under acidic conditions by the same author were found to be larger ranging from ~1μm down to 10nm. The particle size obtained in the present work lies in between the two extremes. The particle morphology has been found to be strongly depended on the synthesis procedure used. [2] This possibly accounts for the intermediate particle sizes obtained in this work which lie between the particle sizes of powders synthesised under acidic and basic conditions. High surface areas were confirmed by BET method which shows a value of ~6.60 ± 0.02 m^2/g for the Ta_2O_5 powder.

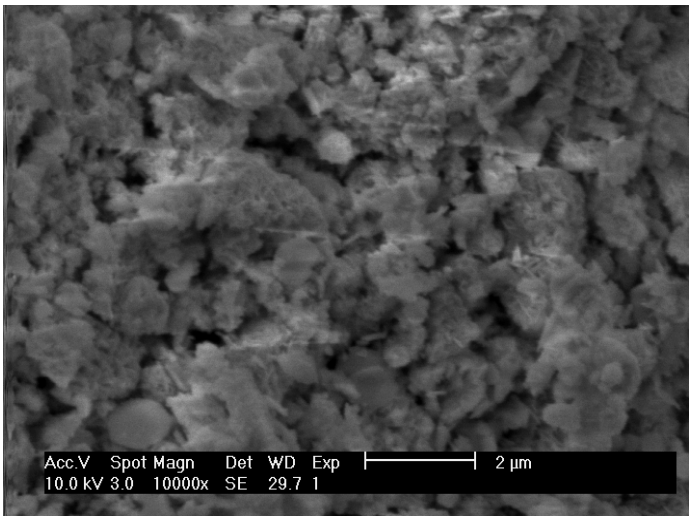

Figure 4.4: SEM micrograph of Ta_2O_5 gel obtained by sol-gel method at 10000x magnification.

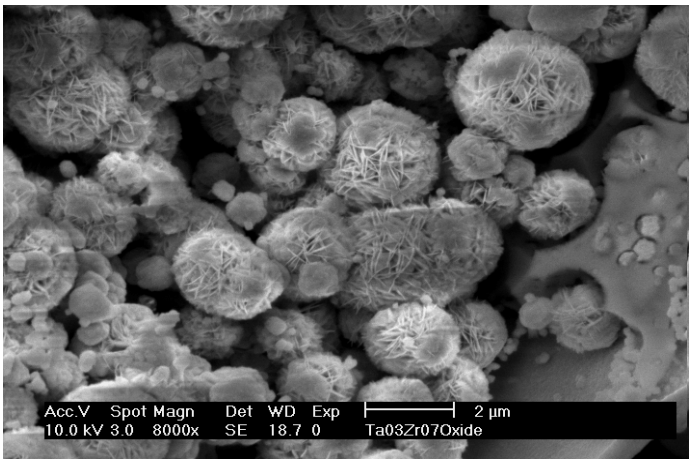

Figure 4.5: SEM micrograph of $Ta_{0.3}Zr_{0.7}$-oxide gel obtained by sol-gel method showing agglomerated submicron needle-like structures at 8000x magnification.

4.2: Thermal nitridation results

Preliminary nitridation done under dry ammonia conditions yielded no oxynitride phases under various conditions of temperature 700-900^{0}C, a heating and cooling rate of 10-20^{0}C/min, nitridation time range of 60-720mins, and ammonia flow rate of 20-50cm^3/min. Ta_3N_5 phase was obtained above 700^{0}C. No TaON phase was obtained under dry ammonia conditions Figure 4.6. This is explained by the low energy requirements for the nitridation reactions as highlighted earlier in Chapter 3.

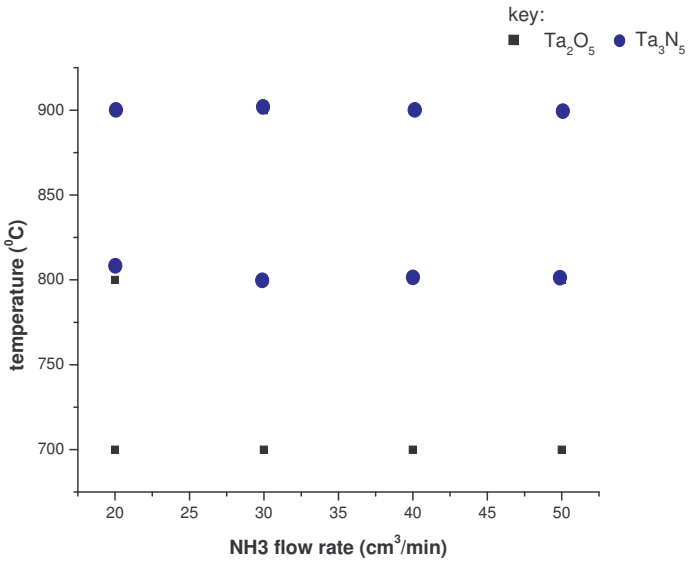

Figure 4.6: An illustration of observed phases obtained at different conditions of temperature and dry ammonia flow rate for 4hrs.

Thermal nitridation under wet ammonia conditions was carried out at varying temperature profiles (700-900^{0}C) and ammonia flow rates (20-50cm^3/min) and yielded different results from the ones observed above, see Figure 4.7. Mixtures of Ta_2O_5 and TaON were observed at temperatures above 700^{0}C and at relatively higher ammonia flow rates (>30cm^3/min). Single phase TaON was observed at 900^{0}C in the ammonia flow rate range of 40-50cm^3/min.

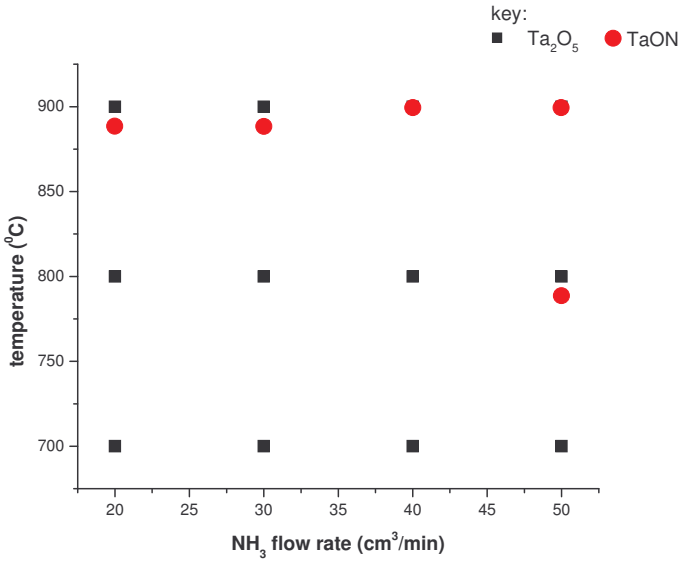

Figure 4.7: A representation of the observed phases prepared at different temperatures and ammonia flow rates for 4h under water vapour.

4.2.1: Nitridation to $Ta_{1-x}Zr_xO_{1+x}N_{1-x}$ phases

Ta-Zr solid solutions with nominal compositions $Ta_{1-x}Zr_xO_{1+x}N_{1-x}$ (x=0.2 and x=0.7) were nitrided at 900^0C with an ammonia flow rate of $50cm^3$/min in wet ammonia for a period of 4hrs with varying heating rates 10-20^0C/min. This condition was obtained from the previous experiments used to nitride Ta_2O_5. The phases formed were analysed by X-ray diffraction and visual inspection.

$Ta_{0.3}Zr_{0.7}O_{1.7}N_{0.3}$ phase:

Pale yellow powders were observed for all nitridation conditions. Nitridation of this phase was found to be highly depended on the heating rate. This is due to the difference in the rates of crystallisation of ZrO_2 and Ta_2O_5. Higher heating rates (>10^0C/min) resulted in decomposition of the solid solution to form monoclinic ZrO_2 and the oxynitride phase (Figure 4.8). This phenomenon has been described previously by Guenther *et al* [13] who observed some monoclinic ZrO_2 deposits for

in the phase system $Ta_{1-x}Zr_xO_{1+x}N_{1-x}$ for $x \geq 0.28$. Two preconditions have been found to be crucial in the successful nitridation of $Ta_{1-x}Zr_xO_{1+x}N_{1-x}$ ($x \geq 0.28$);

i.) a homogeneous distribution of Ta and Zr in the oxide precursor.

ii.) a moderate heating rate ($\leq 10^0$C/min) during nitridation.

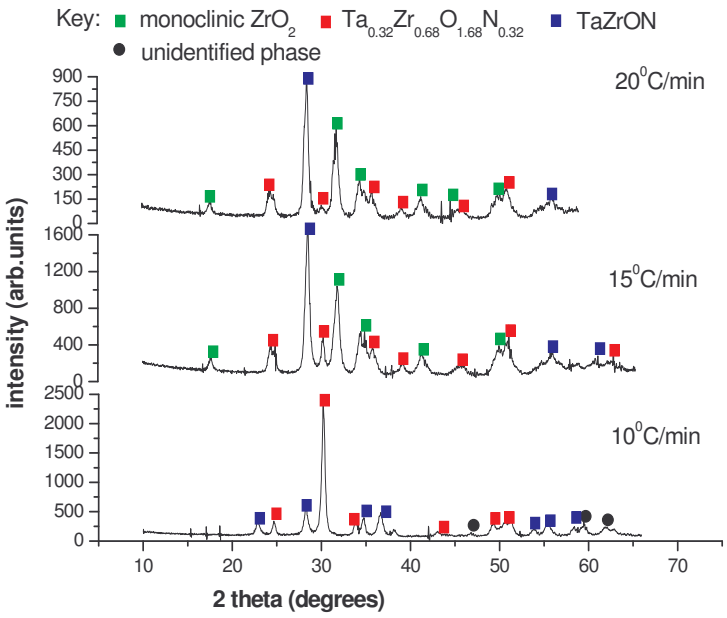

Figure 4.8: XRD patterns of $Ta_{0.3}Zr_{0.7}O_{1.7}N_{0.3}$ showing the effect of heating rate on the stability of the solid solution.

Figure 4.8 above shows peaks of $Ta_{0.3}Zr_{0.7}O_{1.7}N_{0.3}$ obtained at various heating rates (20^0C/min, 15^0C/min and 10^0C/min) to a final temperature of 900^0C maintained for 4hrs at an ammonia flow rate of 50cm^3/min under wet ammonia conditions. The exact peaks corresponding to $Ta_{0.3}Zr_{0.7}O_{1.7}N_{0.3}$ were not available in the database, thus the observed peaks were compared with the nearest set of theoretical peaks $Ta_{0.32}Zr_{0.68}O_{1.68}N_{0.32}$ (ref JCPDS # 00-049-1521). As mentioned above at lower heating rates a complete solid solution is obtained due to lower crystallisation rates which favour the formation of separate crystallised phases.

Thus the nitridation reaction is more controlled by kinetics of the crystallisation of the oxynitrides.

$Ta_{0.8}Zr_{0.2}O_{1.2}N_{0.8}$ phase

Bright yellow X-ray pure powders were obtained at 900^0C using wet ammonia at a flow rate of $50cm^3$/min. No ZrO_2 deposits were observed owing to small amounts of Zr present (x<0.28). The X-ray peaks (observed) were compared to those of TaON (JCPDS card # 70-1193 no file corresponding to the exact composition was found in the database). A shift towards smaller 2 theta values and larger d spacings were observed signifying presence of a foreign atom, Figure 4.9 and Table A1 (Appendix A).

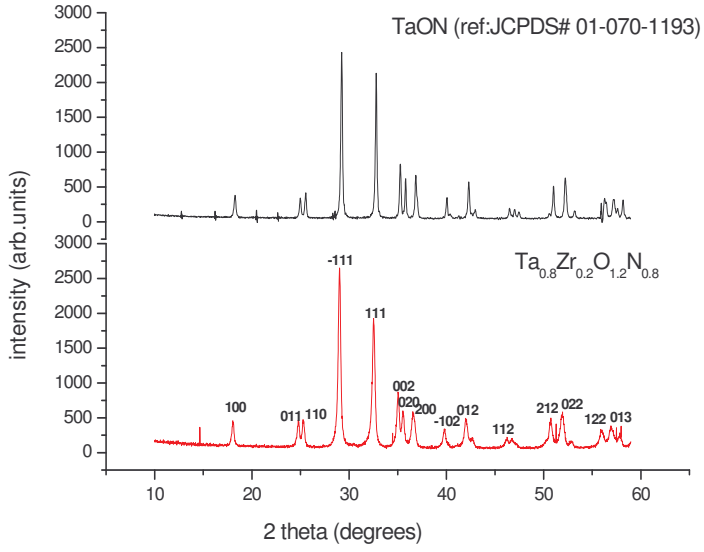

Figure 4.9: XRD peaks of $Ta_{0.8}Zr_{0.2}O_{1.2}N_{0.8}$ powder synthesised at 900^0C,$50cm^3$/min NH_3 flow rate for 4hrs compared to those of monoclinic TaON (ref.JCPDS # 01-070-1193). [2]

4.2.2: Chemical Analysis of oxynitride powders

Tantalum oxynitride has been found to be non-stoichiometric from previous studies. [14, 28] This is due to structural defects encountered in practice, which result in imperfect atomic arrangement in most lattices. The O_2 and N_2 contents of samples nitrided at various times (60-360min) were determined using an ONH analyser. The results obtained are an average of three measurements, as shown below in Table 4.1.

Nitridation time (mins)	Nitrogen (wt%)	Oxygen (wt%)	Formulation
60	3.32±0.02	10.90±0.02	$TaO_{1.44}N_{0.50}$
240	6.77±0.02	7.45±0.02	$TaO_{0.98}N_{1.02}$
360	7.41±0.02	6.81±0.02	$TaO_{0.9}N_{1.12}$
480	6.90±0.02	7.32±0.02	$TaO_{0.97}N_{1.03}$
720	7.03±0.02	7.19±0.02	$TaO_{0.95}N_{1.05}$
Calculated	6.64	7.58	TaON

Table 4.1: Comparison of experimental (ONH analyser) and calculated oxygen and nitrogen contents.

There is a gradual increase in the amount of nitrogen deposited with increasing time. A sharper increase is observed in the range 60min to 240min than between 240min and 360min. The difference is in the number of oxygen sites available for substitution by the nitrogen which decreases with nitridation time. A stoichiometric compound was obtained within 240mins (4hrs) compared to 12hrs or more reported by other researchers.[3, 20, 50] A 6% change in the amount of nitrogen deposited was recorded by doubling the nitridation time from 360mins to 720mins. This shows that the TaON phase had stabilised at lower times.

4.2.3: Particle size analysis of oxynitride phases

The particle sizes of the raw powders were estimated by SEM and measured by Malvern particle size analyser. A d_{90} (cumulative undersize particle size possessed by 90 vol% of the particles) of ~0.25μm was obtained for the TaON raw powder. The SEM, Figure 4.10 micrograph and the particle size graph clearly show little particle aggregation with a narrow particle size distribution as shown in Figure 4.11.

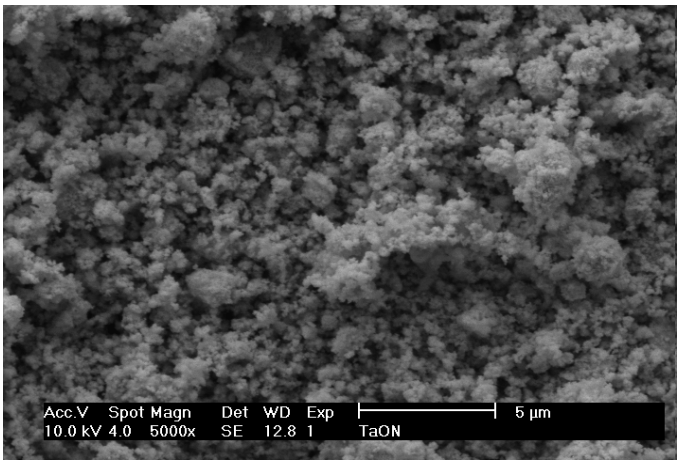

Figure 4.10: SEM micrograph of the TaON raw powder produced by nitridation at 900^0C, 20^0C/min heating rate and an ammonia flow rate of 50cm^3/min.

.

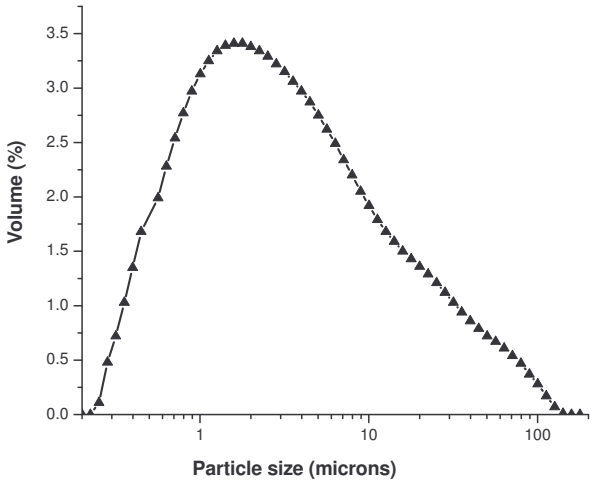

Figure 4.11: Particle size distribution of the TaON raw powder obtained at 900^0C and ammonia flow rate of $50cm^3$/min for 240mins by Malvern particle size Analyser.

However this was not the case with the Ta-Zr oxynitrides (see Figures 4.12 and 4.13). There was some extensive aggregation of the powders to form hard agglomerates which were not completely broken down to fine powders during particle sizing. This resulted in d_{90} values of ~4μm for the $Ta_{0.8}Zr_{0.2}O_{1.2}N_{0.8}$ phase and ~6μm for the $Ta_{0.3}Zr_{0.7}O_{1.7}N_{0.3}$ phase respectively. There is wider particle size distribution in both cases as a result of this agglomeration (see Figure 4.14). The distributions were somewhat bimodal in nature with a skew towards larger sized particles.

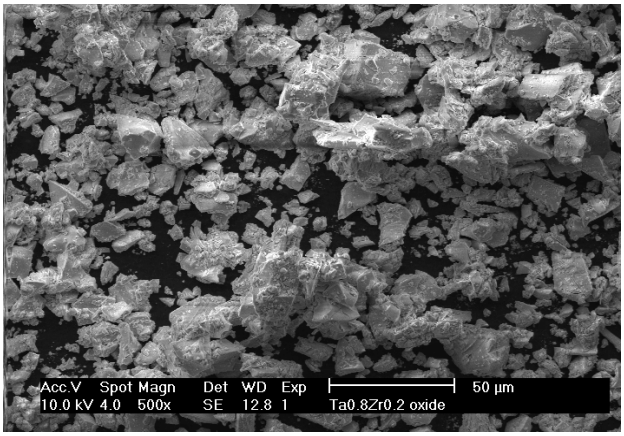

Figure 4.12: SEM micrograph of $Ta_{0.8}Zr_{0.2}O_{1.2}N_{0.8}$ raw powder at 500X magnification produced by sol-gel and calcined at 700^0C for 6hrs.

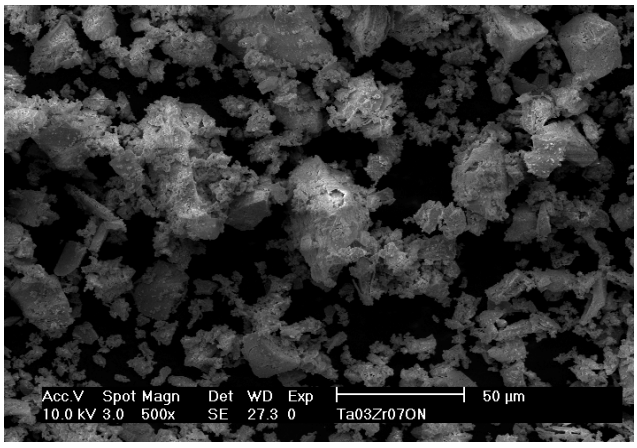

Figure 4.13: SEM micrograph of $Ta_{0.3}Zr_{0.7}O_{1.7}N_{0.3}$ raw powder at 500X magnification produced by sol-gel and calcined at 700^0C for 6hrs.

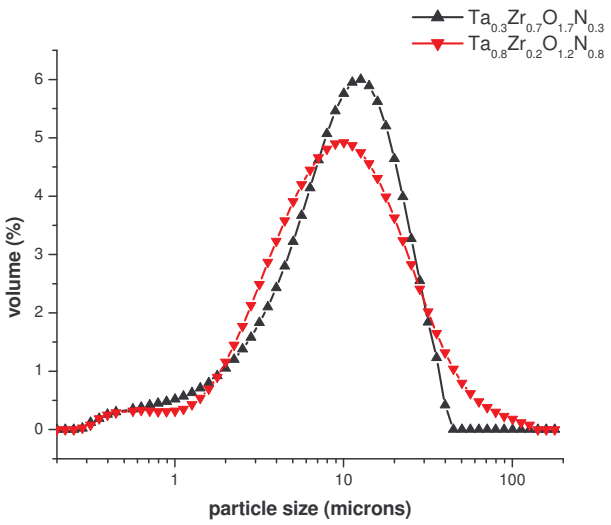

Figure 4.14: Particle size distribution of raw powders of the phases $Ta_{0.8}Zr_{0.2}O_{1.2}N_{0.8}$ and $Ta_{0.3}Zr_{0.7}O_{1.7}N_{0.3}$ produced by nitridation at 900^0C ,heating rate of 10^0C/min for 240mins and measured by Malvern particle size Analyser.

4.2.4: Thermal stability

The thermal stability of the oxynitrides in air and in pure inert and nitrogen gases was investigated by thermogravimetric analysis (TGA). Oxidation was observed in air. The oxidation was mainly due to oxygen uptake to the respective oxides with subsequent weight gain as reflected by Figure 4.15 below. Generally the TaON powder exhibits greater resistance to oxidation up to 690^0C. There is no clearly defined point of oxygen uptake of Ta-Zr oxynitrides with an approximate value of ~600^0C.

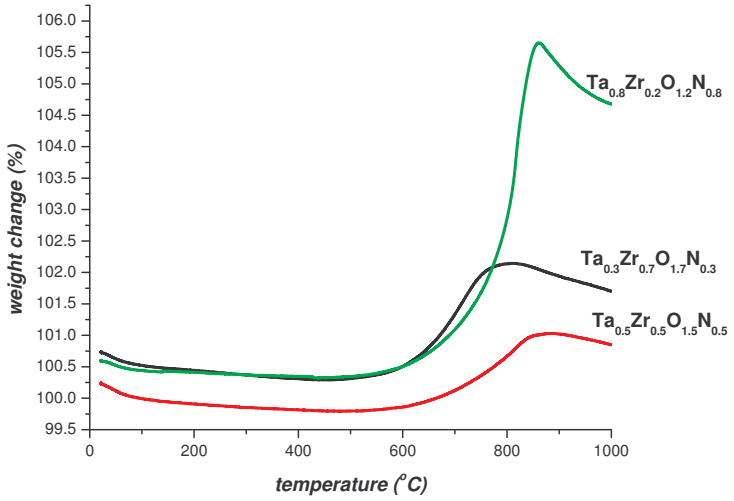

Figure 4.15: Thermal stability in air by TGA of $Ta_{0.3}Zr_{0.7}O_{1.7}N_{0.3}$, $Ta_{0.8}Zr_{0.2}O_{1.2}N_{0.8}$ and $Ta_{0.5}Zr_{0.5}O_{1.5}N_{0.5}$ produced by nitridation at 900^0C in flowing ammonia at a heating rate of 10^0C/min for 240mins.

The oxidation resistance of TaON powder was compared with that of WC-12Co and polycrystalline c-BN powders. Generally it lies in between that of WC-12Co and pc-BN (polycrystalline c-BN), Figure 4.16. This value is slightly higher than the theoretical value of diamond (600^0C).[13] Thus in terms of thermal oxidation the oxynitrides are not superior to cBN for example. This limits their use in applications requiring greater oxidation resistance.

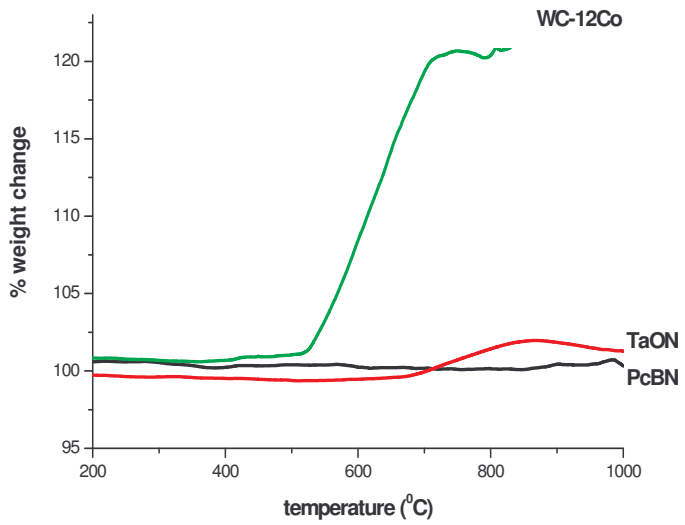

Figure 4.16: Thermal stability of TaON in air in comparison with other hard materials powders.

On the other hand, thermogravimetry done in pure Ar and nitrogen at a heating rate of 10^0C/min up to 1200^0C shows that TaON powder is stable well above 1000^0C, the theoretical decomposition temperature of TaON, signifying stability of the phase in pure environments as shown in Figures 4.17 and 4.18 below.

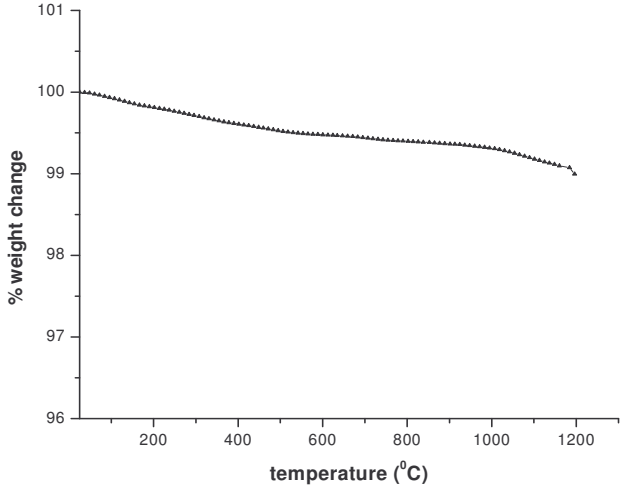

Figure 4.17: TGA results of TaON (900^0C, $50cm^3$/min, 4hrs) in pure argon gas.

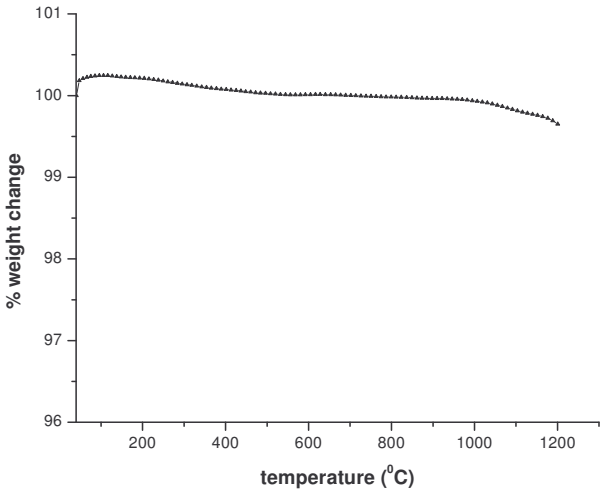

Figure 4.18: TGA results of TaON (900^0C, $50cm^3$/min, 4hrs) in pure nitrogen gas.

However heat treatment experiments carried out in a tube furnace using a silica tube sealed with thread sealer resulted in oxidation of TaON above 1000^0C. This was carried out in pure nitrogen gas (99.99% N_2, *Afrox*) supplied to the furnace without further treatment. Small weight changes and colour changes were noted up to 1200^0C and a complete oxidation was observed at 1400^0C as shown in Table 4.2 below. This indicates that even low partial oxygen pressures result in oxidation.

sample	Temp. (^{0}C)	Initial mass (g)	final mass (g)	%weight change	Phase composition (XRD)
1	1100	1.089±0.02	1.091±0.02	0.18	TaON+Ta_2O_5
2	1200	1.338±0.02	1.343±0.02	0.38	TaON+Ta_2O_5
3	1300	1.400±0.02	1.449±0.02	3.50	Ta_2O_5
4	1400	1.258±0.02	1.312±0.02	4.29	Ta_2O_5

Table 4.2: Heat treatment results of TaON powder in pure nitrogen gas at a heating rate of 10^0C/min in the temperature range 1100^0C -1400^0C.

4.3: Densification and Characterisation of hot pressed materials

The powders were densified by hot pressing using a hot press in the temperature range 900-1400^0C in an inert gas environment. The experiments were done to investigate the stability of TaON at temperatures above 1000^0C. Table 4.3 below shows a summary of the sintering experiments done in nitrogen and argon environments in a temperature range of 900-1400^0C and a sintering pressure range of 50-85MPa for a period of 60minutes. This was done using a 17mm and 10mm internal diameter h-BN crucible in the hot press. The h-BN crucibles used were heat treated at 1800^0C in N_2 for 5hrs prior to sintering to remove any B_2O_3 present. The powders were outgassed in vacuum for 30minutes at 400^0C without pressing. This was followed by subsequent heating to the final temperatures at a

rate of 50^0C/min in a gas environment. A maximum % theoretical density of 81.3% was obtained at a sintering pressure of 50MPa. There is a trend towards higher sintered densities at higher pressures. Oxidation to the respective oxide Ta_2O_5 was observed at temperatures above 1000^0C from X-ray diffraction and visual inspection.

Temp/^{0}C	Pressure/MPa	Gas	Green density (g/cm^3)	Sintered density (g/cm^3)	%theoretical density	Remarks/density
900	50	Ar	4.63	5.27	52.7	Low density
1000	50	Ar	4.83	7.28	72.8	Low density
1000	50	Ar	4.35	6.24	62.4	Low density
1000	60	Ar	4.9	7.88	78.8	Low density
1000	85	Ar	4.93	8.16	81.6	Low density
1200	50	Ar	4.33	6.25	(76.2)	Oxidised/XRD
1400	50	Ar	4.11	7.07	(86.2)	Oxidised/XRD

theoretical density of TaON = 10g/cm^3 and Ta_2O_5 = 8.2g/cm^3

Table 4.3: Summary of results for the samples sintered at various temperatures in the hot press.

4.4:High pressure sintering results

Ultrahigh pressure sintering was opted mainly for two reasons. On the one hand the densities obtained in hot pressing were too low and also it was difficult to control oxidation at temperatures above 1000^0C in the hot press. The powder samples were encapsulated in Ta alloy cups, degassed in vacuum at 715^0C for ~480minutes. The samples were sintered under various conditions of pressure (3-5.5GPa) and a temperature range of ~920-1200^0C under vacuum using a high pressure apparatus and analysed in mechanical properties and phase purity as summarised in Table 4.4 below.

Sample	Sintering temp.(^{0}C)	Pressure (GPa)	Time (mins)	Density (g/cm^3)	Phase purity	Hardness (GPa) (H_{v10})	Fracture toughness MPa.m$^{1/2}$
1	920	5.5	15	9.74	TaON(m)	16.4±1.1	2.6±0.7
2	920	5.5	30	not sintered	TaON(m)	n/a	n/a
3	1100	3	15	9.54	TaON(m)	16.2±0.5	3.8±1.1
4	1100	3	30	9.53	TaON(m)	17.7±0.5	3.9±0.6
5	1200	3	30	-	TaON(m)+ Ta_2O_5	16.9±1.7	2.9±0.4
6	1300	3	30	oxidised	Ta_2O_5	-	-
7	1100	3	30	8.23	$Ta_{0.3}Zr_{0.7}O_{1.3}N_{0.3}$	13.4±1.1	brittle
8	1100	3	30	8.90	$Ta_{0.8}Zr_{0.2}O_{1.2}N_{0.8}$	13.02±0.24	1.78±0.21

N.B: m = monoclinic phase; theoretical density of TaON=10g/cm^3

Table 4.4: Mechanical properties and phase purity obtained for the ultrahigh pressure sintered samples.

The densification of TaON under ultra high pressure (3-5.5GPa) and temperatures of 920-1100^{0}C resulted in a slight increase in the hardness. Alloying TaON with small amounts of Zr did not improve the hardness and no phase transition was observed in all cases. Thus higher symmetry phases cannot be obtained under such conditions. Lower pressure conditions (<5.5GPa) were opted for in the preceding experiments owing to some delamination and cracking of the samples at higher pressures as shown in Figure 4.19. An average hardness value of ~16.8GPa was obtained from the three sintered samples (1, 3 and 4) and an average fracture toughness value of ~3.4MPam$^{1/2}$ was obtained. The introduction of ZrO_2 into the TaON matrix (samples 7 and 8) lowered the mechanical properties of the sintered material. The hardness values obtained for the mixed oxynitrides are comparable to those of ZrO_2 ceramics although the fracture toughness values are inferior.

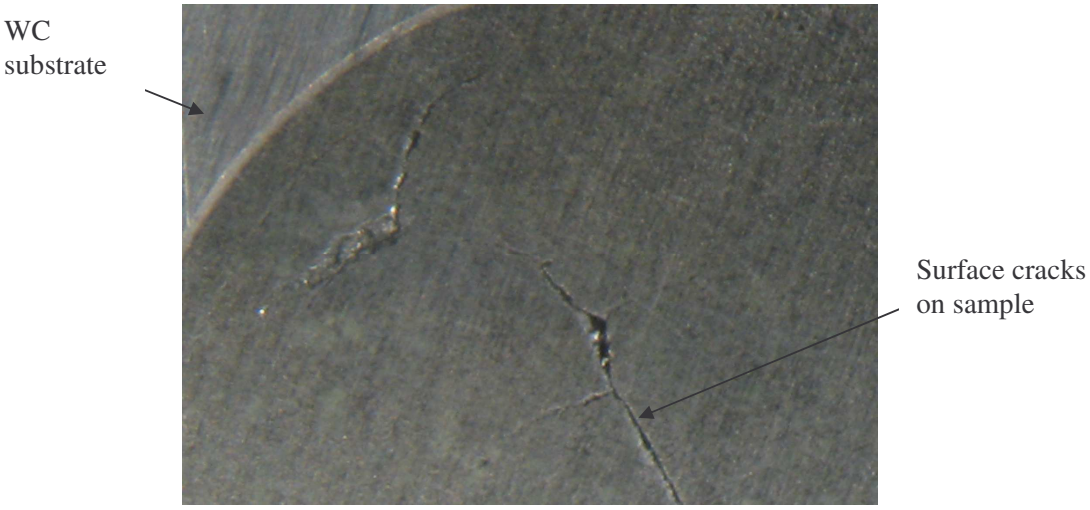

Figure 4.19: SEM micrograph of sample 1 sintered at 5.5GPa and 900^0C using a high pressure apparatus showing surface cracks.

Ta_2O_5 phases were observed at temperatures >1100^0C signifying some oxidation occurring above this temperature. A phase change from beta to alpha Ta_2O_5 was observed at 1300^0C. This was confirmed from the Ta-Ta_2O_5 phase diagram (Figure A1) which shows a β-Ta_2O_5 to α-Ta_2O_5 phase transition at a temperature of ~1320±30^0C. Figure 4.20 below shows the progressive oxidation of TaON with increasing temperature. At 1300^0C a phase change was predicted and some TaN was detected in the samples thus the reactions taking place under vacuum are a combination of decomposition and oxidation. This reflects the low oxidation resistance of the oxynitride at low oxygen partial pressures.

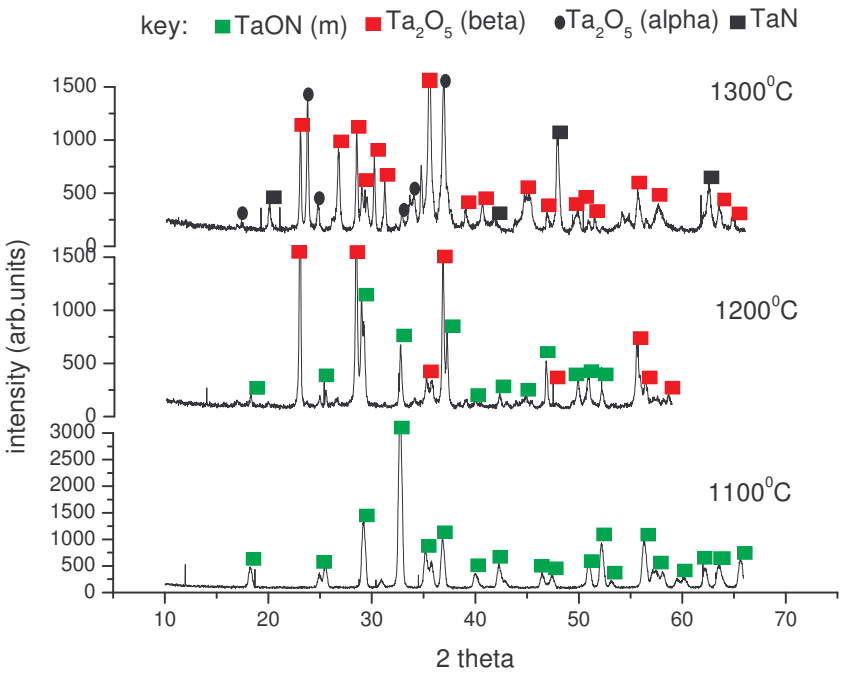

Figure 4.20: XRD peaks of the observed phases showing progressive oxidation at temperatures >1100^{0}C during ultra high pressure sintering.

4.4.2: Microstructural analysis of densified materials

The characteristics of the densified materials were linked with microstructures obtained by SEM. From the polished section of sample 2 it can be seen that the material is completely dense with a few large pores (see Figures 4.21 and 4.22). These pores do not affect the determined properties owing to their small number. The grain size of the materials was approximated to be ~1.5μm from the polished surfaces in Figure 4.22 & 4.23 below.

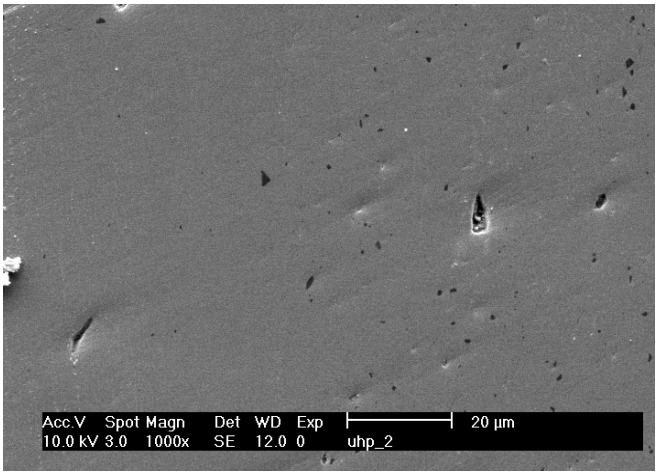

Figure 4.21: SEM micrograph of polished surface of sample 2 sintered at 3GPa and 1100^0C for 15mins at 1000X magnification showing large pores.

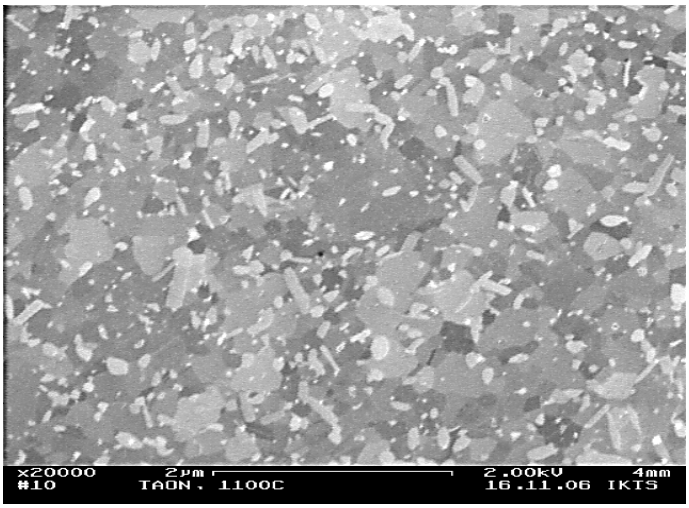

Figure 4.22: SEM micrograph of sample 2 polished surface, sintered at 3GPa and 1100^0C for 15mins at a magnification of 20 000X. The white phases had slightly higher nitrogen content.

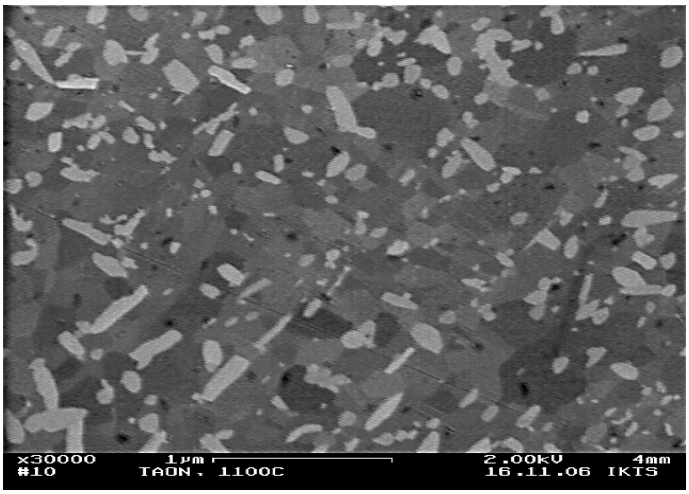

Figure 4.23: SEM micrograph of sample 2 polished surface, sintered at 3GPa and 1100^0C for 15mins at a magnification of 30 000X. The white phases had slightly higher nitrogen content.

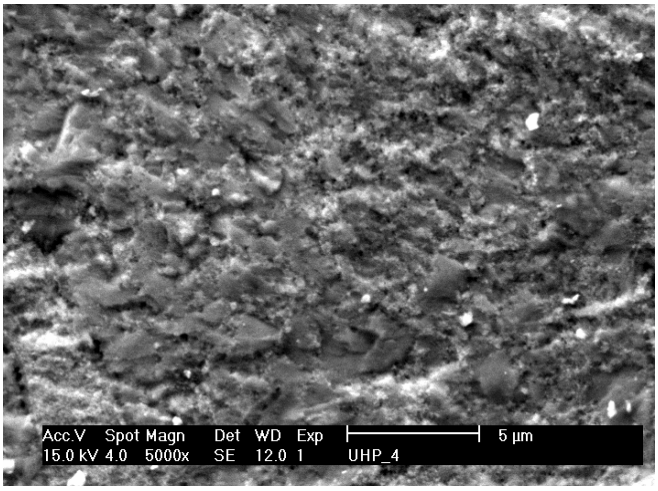

Figure 4.24: SEM micrograph showing fracture surface of $Ta_{0.3}Zr_{0.7}O_{1.3}N_{0.3}$ sintered at 3GPa and 1100^0C for 15 mins (white phases contained some undissolved ZrO_2 phases).

Chapter 5: Conclusion

The potential of TaON as a potential hard material for possible cutting tool application has received much theoretical attention recently with computational approaches being used to predict the hardness values that this phase can attain.[1] The present work was aimed at understanding the fundamental science behind the synthesis of the monoclinic phase of this material and obtaining the high pressure cotunnite phase at commercially available sintering pressures and temperatures. We have extended our studies by examining the effect of alloying TaON with ZrO_2 on the sintering pressure. It was hoped that alloying would lower the monoclinic to cotunnite transition pressure, previously predicted to be 30GPa.[6]

Ta_2O_5 and Zr-Ta oxides were successfully synthesised by a sol gel method. High surface area amorphous powders were obtained using calcination temperatures of $\leq 750^0$C. Thermal nitridation studies were carried out to establish the optimal conditions for the synthesis of the oxynitride phases. The optimal conditions for the synthesis of TaON were found to exist at a temperature of 900^0C and an ammonia flow rate of $50cm^3$/min in the presence of water vapour. Stoichiometric TaON was obtained in a time of 4hrs starting with a powder with a surface area of ~6.60 ± 0.02 m^2/g for the Ta_2O_5 powder. The same conditions were used to obtain $Ta_{0.8}Zr_{0.2}O_{1.2}N_{0.2}$ successfully. However the synthesis of $Ta_{0.3}Zr_{0.7}O_{1.7}N_{0.3}$ was always accompanied by monoclinic ZrO_2 formation. The formation of ZrO_2 was found to be depended on the heating rate. This was investigated at heating rates of 10^0C/min,15^0C/min and 20^0C/min. Complete solid solubility was found to occur at lower heating rates i.e $\leq 10^0$C/min. Guenther *et al*[5] reported on the complete solubility in the phase $Ta_{1-x}Zr_xO_{1+x}N_{1-x}$ to be limited to $x \leq 0.28$. Excess ZrO_2 was found to deposit next to the solid solution phase. Grins *et al*[3] however reported on complete solid solubility up to x=0.4 in $Ta_{1-x}Zr_xO_{1+x}N_{1-x}$ (Table 5.1).

Table 5.1: Compositions of Ta-Zr oxynitrides and nitridation conditions observed by other researchers.

Nominal composition	Composition range	Nitridation conditions ($T/^0C$,f/cm^3/min,t/hr)	Phases obtained	Literature
$Ta_{1-x}Zr_xO_{1+x}N_{1-x}$	$x \leq 0.18$	900^0C,600-1200cm^3/min(dry NH_3),96hrs	Monophasic with a Ta_3N_5 type phase.	[3]
$Ta_{1-x}Zr_xO_{1+x}N_{1-x}$	$0.26 \leq x \leq 0.80$	900^0C,600-1200cm^3/min(dry NH_3),96hrs	Biphasic Ta-Zr solid solution + Ta_3N_5 type phase.	[3]
$Ta_{1-x}Zr_xO_{1+x}N_{1-x}$	$x=0.4$	900^0C,600-1200cm^3/min(dry NH_3),96hrs	Complete solid solution of type $Ta_{0.6}Zr_{0.4}O_{1.4}N_{0.6}$	[3]
$Ta_{1-x}Zr_xO_{1+x}N_{1-x}$	$x=0.9$	900^0C,600-1200cm^3/min(dry NH_3),96hrs	Two phases Ta-Zr baddeleyite phase, with composition close to ZrO_2 + cubic phase.	[3]
$Ta_{3-x}Zr_xO_xN_{5-x}$	$0 \leq x \leq 0.66$	950-1000^0C, various flow rates and dry NH_3 used, 36hrs	Single phase solid solution up to $x=0.28$.	[5]
$Ta_{1-x}Zr_xO_{1+x}N_{1-x}$	$0 \leq x \leq 0.28$	950-1000^0C, various flow rates and dry NH_3 used, 36hrs	Single phase solid solution up to $x=0.28$, m-ZrO_2 deposited at $x>0.28$	[5]

The dependence of TaON formation in the presence of water vapour was investigated. To synthesise pure TaON instead of Ta_3N_5 the use of water vapour pressure in the ammonia according to the equilibrium;

$$3TaON + 2NH_3 = Ta_3N_5 + 3H_2O \quad (5.1)$$

is necessary. In the absence of water vapour a brick red, Ta_3N_5 phase was obtained under conditions of temperatures above 800^0C and ammonia flow rate range of 20-50cm^3/min. X-ray pure TaON was obtained at 50cm^3/min ammonia flow rate at a temperature of 900^0C, a heating rate of 20^0C/min in a time period of 4hrs in the presence of water vapour. The water vapour pressure of such a set up was approximated to be ~$3.14*10^3$Pa. [51]

The oxynitride phases were found to be stable above 1000^0C in pure nitrogen and argon atmospheres using thermogravimetry. Variable temperature experiments carried out in the hot press show lower stability of TaON in a nitrogen atmosphere (<1000^0C). The stability was improved by degassing and sealing the powder in vacuum at 715^0C using a tantalum alloy capsule. The powder was found to be stable up to a temperature of 1100^0C during ultra high pressure sintering in a belt press apparatus. Thus the lower stability in the hot press can largely be attributed to contamination by an impure environment as no encapsulation was done in this case.

TaON like ZrO_2 has a high pressure nine coordinated cotunnite phase theoretically predicted to exist at a pressure of 30GPa.[1,6] The monoclinic phase was found to be stable in the temperature range 920-1100^0C and pressure range of 3-5.5GPa. Alloying of TaON with small amounts of zirconium did not lower the transition pressure in the pressure range investigated. This shows that higher pressures exceeding the commercially available pressures are required to attain this transition pressure. Considering the high cost of high pressure apparatus, achieving this transition is likely to incur a higher cost of production and cost of the material produced

thereof. This defeats the whole purpose of obtaining a cheaper and more useful hard material.

The monoclinic TaON obtained by high pressure sintering at 1100^0C and pressure 3GPa was found to posses an average hardness of ~16.8GPa and a fracture toughness value of ~3.4MPa.$m^{1/2}$. The use of this phase as an abrasive material is limited by the low values in mechanical properties especially the fracture toughness. Owing to the similarities in crystal structures and properties of TaON and ZrO_2 or HfO_2 we were prompted to compare the mechanical properties of the ceramic materials. The hardness values obtained for TaON are higher than those of ZrO_2 or HfO_2 due to stronger covalent bonding of the nitrogen present in TaON. This is well known from other materials, e.g. Si_3N_4 in comparison to SiO_2. The fracture toughness values are as low as those of fully stabilised ZrO_2 materials since there is no phase transformation toughening. A comparison of the three materials is shown in Tables 5.2 and 5.3 below. It is expected that TaON would possess a much higher hardness than ZrO_2 from the bulk moduli values. However the low shear modulus value for TaON contributes to its reduced hardness reflecting different shear planes existing in the baddeleyite structure.

Table 5.2: Comparison of the properties of TaON with ZrO_2-HfO_2 ceramics.

Material	Phases	Vickers Hardness HV(10)	K_{IC}, MPa.$m^{1/2}$	Literature
TaON	monoclinic	16-17	3 -4	This work
Y-TZP	tetragonal/cubic	12.5	8-12	[53]
PSZ (MgO)	tetragonal / cubic	12.5	8-10	[53]
CSY	cubic		2-3	[53]
YTZP (3mol%)	tetragonal / cubic	13.6	13.0 $\pm$ 0.5	[54]
HfO_2 (7mol%)	39% tetragonal/ cubic/60 % monoclinic	14.3	3.8 $\pm$ 0.5	[54]

Table 5.3: Comparison of the calculated Bulk modulus and the shear modulus of different ZrO_2, HfO_2 and TaON phases.

Material	Phases	B (GPa)	G (GPa)	Literature
ZrO_2	Monoclinic	191	-	[1]
ZrO_2	Tetragonal	204	99	[1]
HfO2	Monoclinic	251	-	[55]
TaON	Monoclinic	280	-	[1]
TaON	Tetragonal	242	70	[1]
ZrO_2	Cotunnite	305	-	[55]
ZrO_2	Cotunnite	254	112	[1]
Diamond	Cubic	442-433	524-544	[1]

5.1: Future Work

The present work has been directed towards understanding the chemistry behind the synthesis and sintering of TaON based materials. The greatest challenge that we were faced with, like with other nitride based compounds e.g. Si_3N_4, was the tendency of the phase to oxidise. This made it difficult to vary the temperature by a reasonable margin thus limiting the controllable variables during sintering. Encapsulating in tantalum under vacuum has been found to be an effective method of preventing contamination. It may be possible to sinter these materials at higher temperature by use of sintering additives like in the case of Si_3N_4 ceramics.

References

1. Lowther, J.E. Theoretical Study of Potential High Pressure Phases of TaON and quaternary $ZrTaO_3N$, *Physical Review B*, vol.73, 2006, pp.134110.
2. Fang, C.M., Orhan, E., de Wijs, G.A., Hintzen, H.T., deGroot, R.A., Marchand, R., Saillard, J-Y and deWith, G. The electronic structure of tantalum (oxy)nitrides TaON and Ta_3N_5, *Journal of Materials Chemistry*, vol.11, 2001, pp.1248-1252
3. Grins, J., Kall, P. and Svensson, G. Phases in the $Zr_xTa_{1-x}(O,N)_y$ System, formed by Ammonolysis of Zr-Ta Gels: Preparation of a Baddeleyite-type Solid Solution Phase $Zr_xTa_{1-x}O_{1+x}N_{1-x}$, $0 \leq x \leq 1$, *Journal of Materials Chemistry,* vol.4, issue 8, 1994, pp. 1293-1301.
4. Kerlau, M., Merdrignac-Conanec, O., Guilloux-Viry, M. and Perrin, A. Synthesis of crystallised TaON and Ta_3N_5 by nitridation of Ta_2O_5 thin films grown by pulsed laser deposition, *Solid State Sciences,* vol.6, 2004, pp.101-107.
5. Guenther, E. and Jansen, M. Optical properties of $Ta_{(3-x)}Zr_{(x)}N_{(5-x)}O_{(x)}$ semiconductor pigments, *Materials Research Bulletin*, vol.36, 2001, pp.1399-1405.
6. Lumey, M-W. and Dronskowski, R. First Principles Electronic Structure, Chemical Bonding, and High-Pressure Phase Prediction of the Oxynitrides of Vanadium, Niobium, and Tantalum, *Zeitshrift für anorganische und allgemeine Chemie*, vol.631, 2005, pp. 887-893.
7. Dronskowski, R. Research on Solid State Chemistry. INTERNET . http: // www.ssc.rwth-aachen.de, (2005).
8. Bailey, M.W. Introduction: Novel Ultrahard Materials, *in Handbook of Ceramic Hard Materials,* edited by Riedel R. Wiley- VCH, Weinheim, Germany, vol. 2**,** 2000, pp.480-485.

9. Sholonjenko, V.L., Dub, S.N., and Novikov, N.V. Mechanical properties of cubic BC_2N, a new superhard phase, *Diamond and Related Materials.,* vol.10, 2001, pp.2228.

10. Lumey, M-W. and Dronskowski, R. The electronic structure of Tantalum Oxynitride & Falsification of α-TaON, *Zeitschrift für anorganische und allgemeine Chemie(Journal of Inorganic and General Chemistry),* vol.629, 2003, pp. 2173-2179.

11. Cohen, M.L. Atomic theory of hard crystals, *Journal of Hard Materials*, vol.2, no.1-2, 1991, pp.13-27.

12. Swisher, J.H. and Read, M.H. Thermodynamic Properties and Electrical Conductivity of Ta_3N_5 and TaON, *Metallurgical Transactions*, vol.3, 1972, pp.489-494.

13. Davies, G.J. The Crystallisation of Diamond, *Handbook of Ceramic Hard Materials edited by R.Riedel,* Wiley- VCH, Weinheim, Germany, vol.2**,** 2000 , pp.485.

14. Misra, E., Wang,Y., Theodore, N.D. and Alford, T.L. Evaluation of diffusion barrier and electrical properties of tantalum oxynitride thin films for silver metallization, *Thin Solid films*, vol.457, no.2, 2004, pp.338-345.

15. Ayerdi, I., Castano, E., Garcia-Alonso, A. and Gracia, F.J. Characterisation of tantalum oxynitride thin films as high temperature strain gauges, *Sensors and Actuators*, A 46-47, 1995, pp.218-221.

16. Venkataraj, S., Severin, D., Mohamed, S.H., Ngaruiya, J., Kappertz, O. and Wuttig, M.Towards understanding the superior properties of transition metal oxynitrides prepared by reactive DC magnetron sputtering, *Thin Solid films*, vol.502, no.1-2, 2005, pp. 228-234.

17. Brauer, G. and Weidlein, J.R. Synthesis and properties of Tantalum oxynitride TaON, *Angewandte Chemie International Edition*, vol.4, 1965, pp.241.

18. Ngaruiya, J.M., Kappertz, O., Liesch, C., Muller, P., and Dronskowski, R. Composition and formation mechanism of zirconium oxynitride films produced by reactive direct current magnetron sputtering, *Physica Status Solidi (a)*,vol.201, no.5, 2004, pp.967-976.

19. Tessier, F. and Marchand, R. Ternary and higher order rare-earth nitride materials: synthesis and characterisation of ionic-covalent oxynitride powders, *Journal of Solid State Chemistry*, vol.171, 2003, pp.143-151.
20. Orhan, E., Tessier, F. and Marchand, R. Synthesis and energetics of yellow TaON, *Solid State Sciences*, vol. 4, 2002, pp.1071-1076.
21. Armytage, D. and Fender, B.E.F. Anion ordering in NaON: a powder neutron-diffraction investigation, *Acta Crystallographica*, vol.30, sect.B, 1974, pp.809.
22. King, B.W., Schultz, J., Durbin, E.A. and Duckworth, W.H. Properties of Tantala Systems, *US Army Environmental Centre, BMI*-1106, 1956, pp.1-40.
23. Lerch, M. and Lerch, J. Nitrogen incorporation into Ta_2O_5-containing zirconia ceramics, *Journal of Materials Science Letters*, vol.16, no.17, 1997, pp.1454-1456.
24. Seagal, D. Chemical synthesis of ceramic materials, *Journal of Materials Chemistry*, vol.7, no.8, 1997, pp.1297-1305.
25. Rahaman, M.N. *Ceramic Processing and Sintering*, 2nd edition, Marcel Dekker, New York, USA, 1995, pp.254-270.
26. Reed, J.S. *Principles of Ceramics Processing 2nd Edition,* John Wiley & Sons Inc., New York, USA, 1995 pp.64-80.
27. Mauritz, K.Sol-Gel Chemistry.INTERNET. http: // www.psrc.usm.edu/ mauritz/solgel.html, (2005).
28. Katsura, M. Thermodynamics of nitride and hydride formation by the reaction of metals with flowing NH_3, *Journal of Alloys and Compounds*, vol.182, 1992, pp.91-102.
29. Dong, W. and Dunn, B. Sol-gel synthesis of monoclinic molybdenum oxide aerogels and xerogels, *Journal of Materials Chemistry*, vol.8, no.3, 1998, pp.665-670.
30. Sasa, T. High –Temperature, High-Strength Ceramics, *in Handbook of Advanced Ceramics: Processing and their Applications,* edited by Somiya, S., Aldinger, F., Claussen, N., Spriggs, R.M, Uchino, K., Koumoto, K. and Kaneno, M. Elsevier Academic Press UK, vol 2, 2003, pp.267-271.

31. Tatli, Z. and Thompson, D.P. Densification behaviour of oxide-coated silicon nitride powders, *Materials Letters*, vol.59, issue 14-15, 2005, 1897-1901.
32. Hall, H.T. Ultra-High-Pressure, High-Temperature Apparatus: the "Belt", *Scientific Instruments*, vol.31, issue 2, 1960, pp.125-131.
33. Pagh, H.L.D., McCormic, P.G. and Rouff, A.L. *Mechanical behaviour of materials under pressure, Creep under high pressure,* Elsevier publishing, Amsterdam, 1970, pp.355-356.
34. Chiang, Y., Birnie, D.P. and Kingery, W.D. *Physical Ceramics,* J.Wiley, New York, 1997, pp 39-45.
35. Morrell, R. *Handbook of Properties of Technical Engineering Ceramics Part1: An introduction for the Engineer and Designer*, vol.2, Manchester, UK, 1985, pp.68-69; 92-100.
36. Zerr, A. and Riedel, R. Novel Ultrahard Materials, *in Handbook of Ceramic Hard Materials,* edited by Riedel, R. Wiley- VCH, Weinheim, Germany, vol. 2**,** 2000, pp.XLVI-XLVIII.
37. Munz, D. and Fett, D. *Ceramics: Mechanical properties, failure behaviour, materials selection*, vol 36, Springer, New York, USA, 1999, pp.1-10.
38. Olagnon, C. Chevalier, J. and Pauchard, V. Global description of crack propagation in ceramics, *Journal of the European Ceramic Society*, vol. 26, issue 15, 2006, pp.3051-3059.
39. Evans, A.G. and Charles, E.A. Fracture Toughness Determinations by Indentation, *Journal of American Ceramic Society*, vol. 59, issue 7-8, 1976, pp.371-372.
40. Niihara, K., Morena, R. and Hasselman, D.P.H. Evaluation ofK_{IC} of brittle solids by the indentation method with low crack-to-indent ratios, *Journal of Materials Science Letters*, vol.1, no.1, 1982, pp.13-16.
41. Anstis, G.R., Chantikul, P., Lawn, P. and Marshall, B.R. A Critical Evaluation of Indentation Techniques for Measuring Fracture Toughness: II, Strength Method, *Journal of American Ceramic Society,* vol.64, issue 9, 1981, pp.533-538.

42. Shetty, D.K. and Wright, J.G. Indentation fracture of WC-Co cermets *J.Materials Science*, vol.20, no.5, 1985, pp.1873-1882.
43. Elssner, G., Hoven, H., Kiessler, G. and Wellner, P. *Ceramics and ceramic composites: materialographic preparation*, Elsevier, Amsterdam, Netherlands, 1999, pp.33-61.
44. Jones, M.I., Hirao, K., Hyuga, H., Yamauchi, Y., Shen, Z. and Nygren, M.Wear properties of self-reinforced α-SiAlON ceramics produced by spark plasma sintering, *Wear*, vol.257, issues 3-4, 2004, pp.292-296.
45. Hsu, S. and Shen, M. Wear prediction of ceramics, *Wear*, vol.256, issues 9-10, 2004, pp.867-878.
46. Passaribu, H.R., Sloetjes J.W. and Schipper, D.J. The transition of mild to severe wear of ceramics, *Wear*, vol.256, issue 6, 2004, pp.585-591.
47. Lawn, B.R. Erosion and Wear of Ceramics, *Proceedings of Conference on Wear-Principles and Prevention,* 1980, pp.1-7.
48. Zhou, F., Adachi, K. and Kato, K. Friction and wear behaviour of BCN coatings sliding against ceramic and steel balls in various environments, *Wear*, vol. 261, issues 3-4, 2006, pp.301-310.
49. Pfeiffer, H., Bosch, P. and Bulbulian, S. Sol–gel synthesis of $Li_2ZrSi_6O_{15}$ powders, *Journal of Materials Chemistry*, 2000, vol.10, pp.1255-1258.
50. Houmes, J.D. and Conrad zur Loye, H. Iron-Promoted Synthesis of Tantalum and Niobium Oxynitrides, *Journal of Solid State Chemistry*, vol.127, issue 2, 1996, pp.267-275.
51. Hall, J.R. and Brouillard, R. Water vapour pressure calculation, *Journal of Applied Physiology*, vol.58, 1985, pp.2090.
52. Garg, S.P., Krishnamurthy, N., Awasthi, A.and Venkatraman, M. Assessed diagram of the region Ta-Ta_2O_5, *J.Phase Equilib.,* vol.17, no.1, 1996, pp.63.
53. Brevier Technische Keramik (Brevier Technical Ceramics), Verband der Keramischen Industrie e.V, 2003.
54. Mojaki, E. *PhD Thesis*, University of the Witwatersrand, Johannesburg, 2004.

55. Lowther, J.E., Dewhurst, J.K., Leger, J.M.and Haines, J. Relative stability of ZrO_2 and HfO_2 structural phases, *Phy.Review B*, vol. 60, 1999, pp.14 485.

APPENDIX A

2θ theoretical (^{0})	2θ observed (^{0})	d_{hkl} observed (Å)	hkl	d_{hkl} theoretical[a] (Å)
18.093	18.051	4.910	100	4.888
24.845	24.769	3.591	011	3.580
25.396	25.276	3.520	110	3.504
29.107	28.997	3.076	-111	3.065
32.665	32.503	2.752	111	2.739
35.150	35.024	2.559	002	2.551
35.695	35.522	2.524	020	2.513

[a] *standard powder diffraction data for TaON(ref.JCPDS # 01-070-1193)*

Table A1 : Comparison of theoretical and observed powder diffraction data for $Ta_{0.8}Zr_{0.2}O_{1.2}N_{0.8}$.

2θ theoretical (^{0})	2θ observed (^{0})	d_{hkl} observed (Å)	hkl	d_{hkl} theoretical[a] (Å)
18.134	18.172	4.859	100	4.888
24.845	24.901	3.573	011	3.580
25.396	25.484	3.492	110	3.504
29.107	29.174	3.059	-111	3.065
32.665	32.720	2.735	111	2.739
35.150	35.158	2.550	002	2.551
35.695	35.729	2.511	020	2.513

Table A2: Comparison of theoretical and observed powder diffraction data for TaON.

APPENDIX B

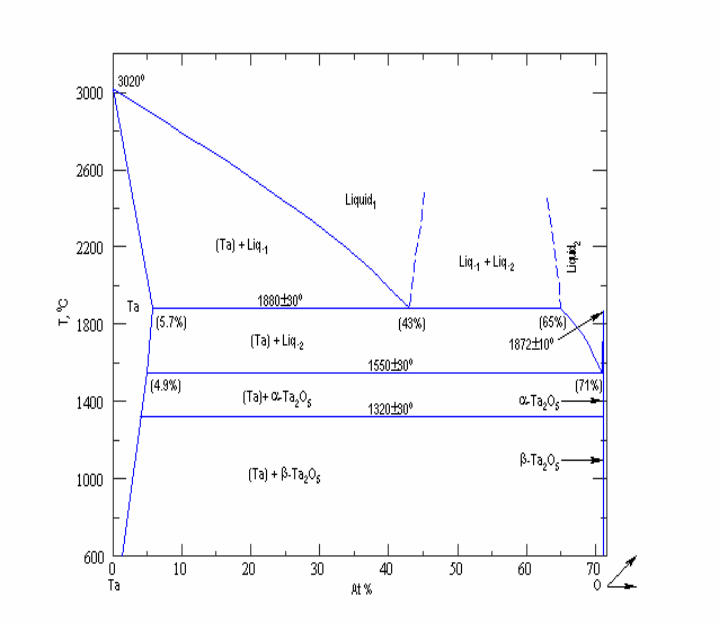

Figure B1: Ta-Ta_2O_5 phase diagram.[52]